6th BSME International Conference on Thermal Engineering (ICTE 2014)

Winglet Type Dielectric Barrier Discharge Plasma Actuators: Performance Characterization and Numerical Comparison

A.N.M. Mominul Islam Mukut[a]*, Hiroshi Mizunuma[b], Obara Hiromichi[b] and Takehiko Segawa[c]

[a]Dhaka University of Engineering & Technology (DUET), Gazipur-1700, Bangladesh
[b]Tokyo Metropolitan University, Tokyo 192-0397, Japan
[c]National Institute of Advanced Industrial Science and Technology (AIST), Tsukuba, Japan

Abstract

Winglet type dielectric barrier discharge plasma actuator (PA) with two exposed electrodes have been investigated experimentally in a quiescent air and numerically modeled. Three arrangement of electrode positions are used: leading edge type (here after L PA), middle edge type (here after M PA), and trailing edge type (here after T PA) to investigate the effect of electrode position on induced flow. When the electrodes are located at the leading edge of the winglet PA, the stream wise flow is effectively enhanced on the covered electrode; on the other hand when the electrodes are located at the trailing edge, the friction loss is minimized for the near-wall high shear flow over the winglet and thus the highest momentum integral is obtained for the downstream jet-like flow. As all three type of PAs have two exposed electrodes, hence two separate jet flows are induced which are unified to a single jet after the winglet trailing edge. The electrode location also influences the unification velocity at downstream. The longer distance between trailing edge and embedded electrode reduces the downstream unified velocity. Particle image velocimetry (PIV) technique has been implemented to investigate the flow field. Simulation results are found to be consistent and in good agreement with experimental data.
© 2015 The Authors. Published by Elsevier Ltd.
Peer-review under responsibility of organizing committee of the 6th BSME International Conference on Thermal Engineering (ICTE 2014).

Keywords: dielectric barrier discharge plasma actuator; velocity profile; flow control; PIV; jet; CFD

* Corresponding author. Tel.: +88-02-9204710; fax: +88-02-9204710-.
  E-mail address: mukut@duet.ac.bd

1. Introduction

Plasma actuators are a kind of aerodynamic flow control actuators which get tremendous research interest for more than a decade as they require no moving parts, easier to construct and control, low power consumption. These actuators hold promise for airfoil leading edge separation control [1,2], control of airfoil dynamic stall [3], bluff body flow control [4,5], boundary layer flow control [6,7], high-lift applications [8], turbo machinery flow control [9,10] and so on. A simple plasma actuator is consists of two electrodes that are separated by a dielectric material.

Nomenclature	
ϕ	electric potential
ρ_c	charged particle density
$\overrightarrow{f_b}$	body force
ε_r	relative permittivity
U_{max}	peak velocity at streamwise locations

The electrodes are supplied with an AC voltage with enough magnitude which ionize the air over the covered electrode which is also known as embedded or grounded electrode. Here the term ionized referred as plasma, that's why they are referred as plasma actuator. The word ''plasma'' was introduced into the physics literature by Langmuir [11] to denote an electrically neutral region of gas discharge. The ionized air, in the presence of the electric field produced by the electrode geometry produce a body force vector that acts on the ambient (neutrally charged) air. The body force is the mechanism for active aerodynamic control.

The plasma actuator is thin and controllable electrically. Until now, the actuators have been mounted on the wall surface. For example, a vortex generator is located on the wall surface and LEBU (Large Eddy Break Up) device is located with some distance from the wall surface. These devices are composed of thin plates which are requested to have simple structure and minimum sizes. Thus the applications are limited to passive flow control. On the other hand, the DBD plasma actuator has a function of the active control in spite of its simple structure. Thus if the combination of those passive control devices and the DBD plasma actuator is possible, it is expected to bring a new active method for the flow control. From this point of view, a plate-like plasma actuator located with a distance from the wall surface has been developed. In this paper three type of plasma actuators are numerically and experimentally evaluated to figure out their effectiveness so that they can be used as vortex generator to control flow separation.

2. Method

2.1. Experimental setup

All of three types of plasma actuators have been investigated here have two exposed electrodes on both sides with common embedded electrode as shown in figure 1; convectional two plasma actuators have been glued together to make such special type of plasma actuators. The width and chord length of mini-plate wing were 96 mm and 19.6 mm respectively. The electric wind was generated in the absence of external flow by the plasma actuator. Exposed and embedded (grounded) electrodes were separated by a Kapton thin wing plate. Detailed dimension (all in mm) have been shown in figure 1. The induced flow was compared as a function of the distance from the leading edge to the actuator position. Due to use of two exposed electrodes plasma was created on both sides of actuator surfaces. All experiments were carried out with a frequency of 5 kHz and the corresponding applied voltage were 2.5kV, 3kV, 3.5kV and 4kV respectively. All experiments were carried out in absence of external air flow.

Particle image velocimetry (PIV) was employed to quantify the behavior of the flow field during testing at AIST Tsukuba [12]. A horizontal laser sheet would strike at the midpoint of the plasma actuator from downstream, so that

only suction side was in shadow which helped to measure a two dimensional cross-section of the flow field around the airfoil. The schematic diagram of PIV experiment is presented in figure 2.
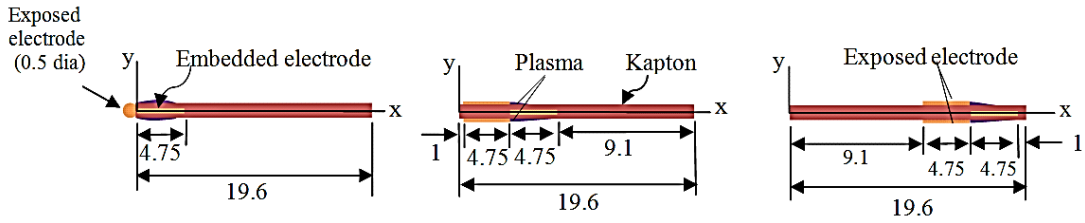

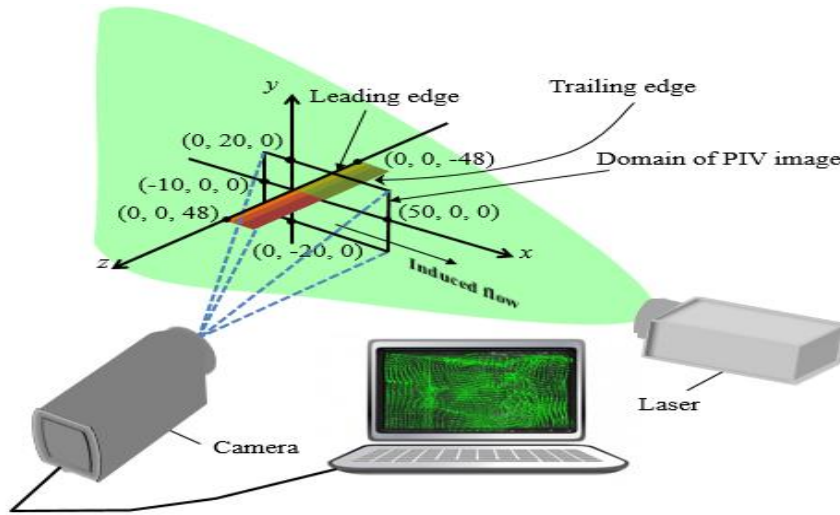Fig. 1. Plasma actuator geometry (a) L PA (b) M PA (c) T PA (all dimension in mm)

Fig. 2. PIV setup

2.2. Numerical model

A numerical model for the PAs is useful to optimize their performance. As plasma were created both side of PAs tested, hence it was quite difficult to get detailed flow information near the electrode positions due to low spatial resolution of PIV images. In this regard numerical simulation is effective to explore near electrode flow filed. Hence numerical modeling and simulation has been carried out based on Suzen Model [13].

The governing equations are given below:

$$\frac{\partial u}{\partial x} + \frac{\partial u}{\partial y} = 0 \tag{1}$$

$$\frac{DU}{Dt} = -\frac{1}{\rho}\nabla p + \mu\nabla^2 U + \overrightarrow{f_B} \tag{2}$$

The above mentioned two dimensional Navier-Stokes equation and continuity equation were solved with the electric potential, which was divided into two potentials. One is a potential due to the external electric field $\varphi\,(t, x, y)$ and the other is a potential due to the net charge density $\rho_c\,(t, x, y)$.

$$\nabla(\epsilon_r \, \nabla\emptyset) = 0 \qquad\qquad (3)$$

$$\nabla(\epsilon_r \, \nabla\rho_c) = \frac{\rho_c}{\lambda_d{}^2} \qquad\qquad (4)$$

Where ε_r is the relative permittivity and λ_d is the Debye length. A finite volume method was used to compute the equations. In computation, the electrical potential φ and the particle charge density ρ_c were calculated at first. Then, these values were used to calculate the electro-hydrodynamic force, which was integrated into the flow equations. PHOENICS (CHAM-Japan) was used as the solver. The computational domain was 60 mm ×40 mm and same as that of PIV. The total number of computational meshes was 95 ×91. All computations assumed laminar flow and the average was calculated to compare those with the time averaged result of PIV.

3. Result and discussion

Downstream unification of two separate induced flows were clear and well match in both experiment and simulation; to clarify it, peak velocity have been shown in figure 3. Comparison of experimental and simulated velocity profiles have been plotted at x=30mm and is presented in figure 4 for 4kV applied voltage only. Velocity profiles from simulation showed two peaks which were absent in experimental velocity profiles this is because in simulation mesh grid is too smaller than experimental measuring grid and spatial resolution of PIV image was low, as a result two peaks clearly appeared in simulation.
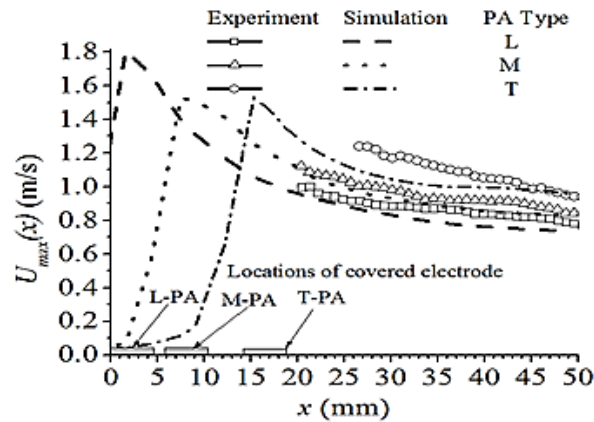

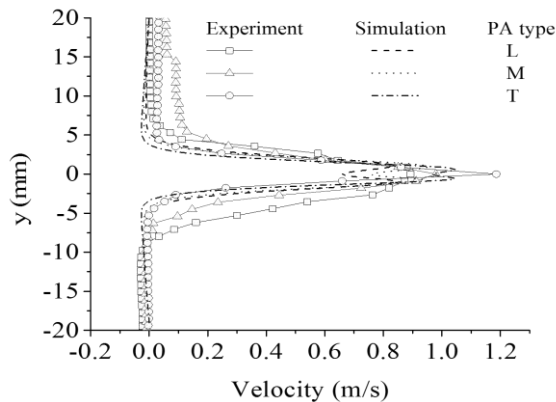Fig. 3. Peak velocity U_{max} as a function of x.

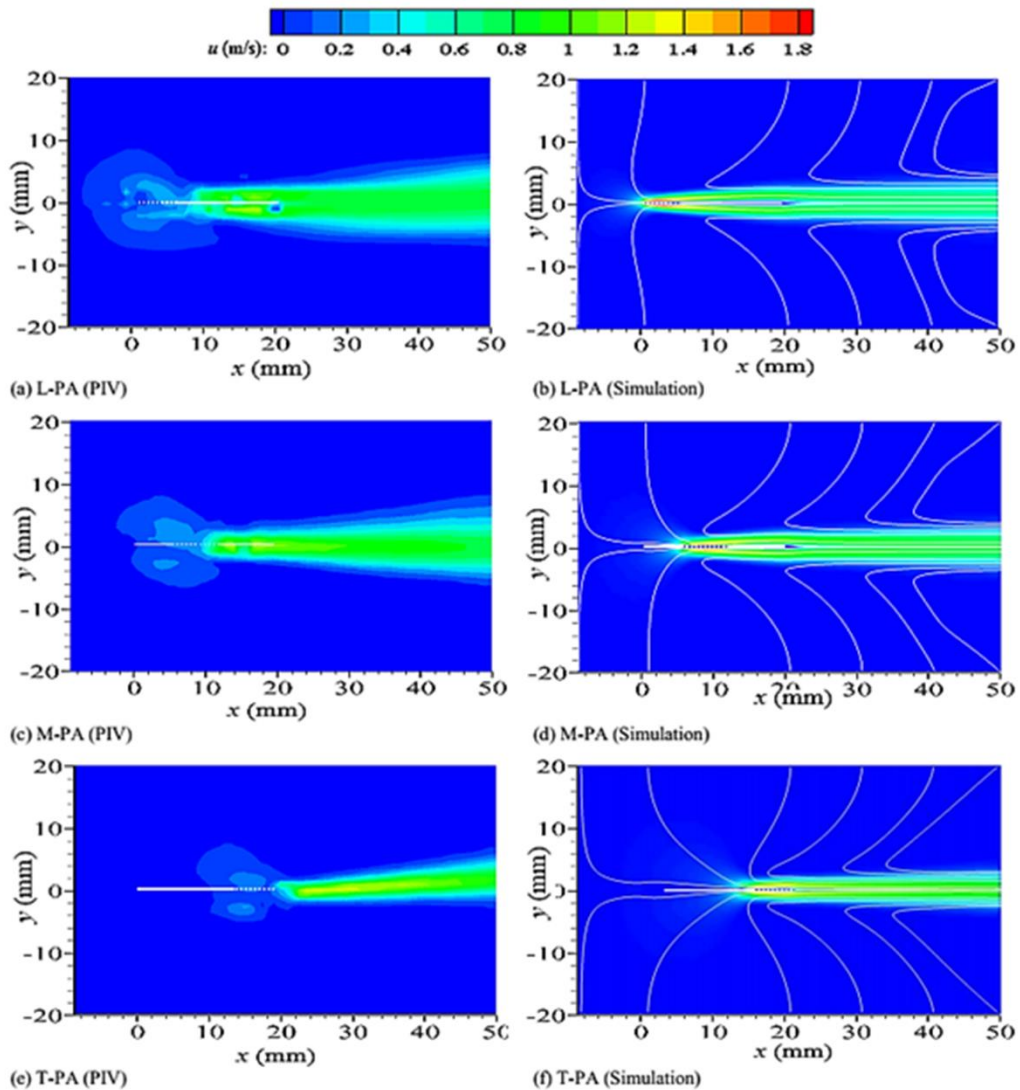Fig. 4. Simulated and experimental velocity profile [voltage amplitude is ±4kV]

Fig. 5. Velocity contour maps around winglets: (a), (c), and (e) PIV measurements, and (b), (d), and (f) computational results. The applied voltage is ±4 kV. The dotted line indicates the location of covered electrode.

The result of PIV measurements which is shown in figure 5, it is found that the maximum velocity U_{max} was located more downstream and the maximum velocity was less than that in the computational result. These differences are because the PIV does not have enough high spatial resolution near wall and the velocity peak is smeared in the near-wall thin shear flow over the covered electrode. In the jet flow region, the computed velocity contour maps showed the similar results as those of the PIV measurements. Both experiment and simulation indicate wider jet width like L>M>T PA. This is because the electrode arrangement on mini wing plate.

Figure 6 represents the maximum induced flow velocity for each type of PA with corresponding applied voltage to figure out the effect of applied voltage on induced flow velocity. The induced velocity increases with the voltage because the electric field also increases and ions undergo higher Columbian forces [14].
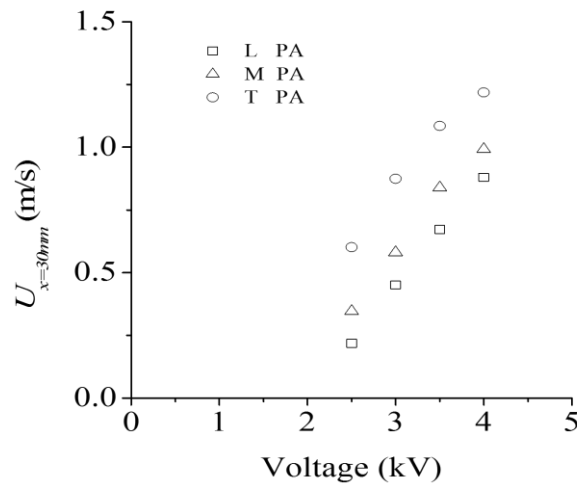
Fig. 6. Change of induced velocity (at x=30mm) with applied voltage

Behavior of near electrode flow has been investigated easily from simulation. M and T PA have same shape of electrode except location over plate, gave same trend of induced flow but M PA provides lower induced flow at trailing edge than T PA.

On the other hand, L PA gives maximum induced velocity than M and T PA but at downstream unified velocity is lower than other two types. Trend of flow reduction over embedded electrode has been shown from computed results in figure 7 based on peak velocity at each x locations.
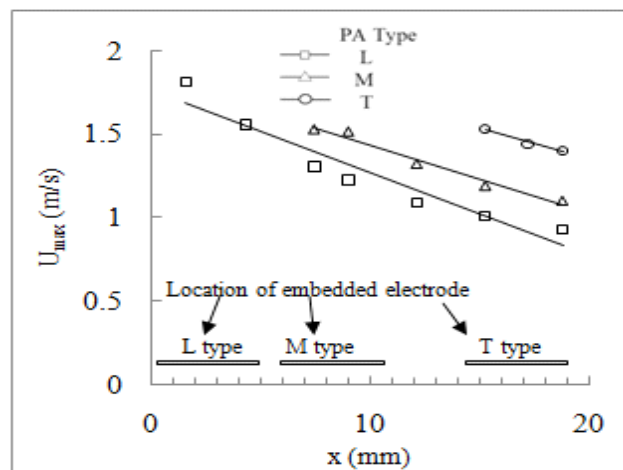

Fig. 7. Trend of flow reduction over wing

The reason is the end gap between the embedded electrode and trailing edge of wing. Higher the end gap increase frictional loss which reduces downstream flow. In all three types of PA, maximum induced flow has been found at 0.44mm above (both side) of actuator surface. Along this y location, percentage of flow reduction has been calculated from velocity changes along x axis and presented at table 1.

Table 1. Calculation of flow reduction over wing

Type of actuator	Max. induced flow velocity (m/s)	Velocity at the end of wing plate (m/s)	% of flow reduction
L PA	1.81	0.35	80.51%
M PA	1.53	0.599	60.74%
T PA	1.53	1.2	21.597%

It is found that increase in distance between embedded electrode and tailing edge of wing, decrease the induced velocity at the end of tailing edge as a result lower unified velocity at downstream

4. Conclusion

In this paper, experimental analysis and numerical modelling have been performed to evaluate special design plasma actuator. Effect of end gap and shape of exposed electrodes have been investigated. From the above mentioned analyses it is clear that velocity reduction over wing is less for that type of PA which has smallest gap between embedded electrode and trailing edge. Higher the gap higher the reduction at downstream. As a result lowest velocity reduction has been found in T PA and higher unified velocity at downstream than other two types of PA. Shape of exposed electrode has a great role on near electrode flow. Only L PA has wire type exposed electrode, from simulation it is found that this type of PA provides maximum induced flow over embedded electrode than that of M PA and T PA as shape of exposed electrode is different. Both M PA and T PA have same shape of exposed electrode but only difference is in electrode position on mini-plate wing and both of these PA gave same magnitude of induced flow velocity. So, it is clear that shape of exposed electrode has a great influence on induced flow.

Acknowledgements

References

[1] M. L. Post, and T. C. Corke, Separation control on a high angle of attack airfoil using plasma actuators, J. AIAA. 42(2004) 2177–2184
[2] N. Benard, P. Braud, and J. Jolibois, airflow reattachment along a NACA 0015 airfoil by surface SDBD actuator-time resolved PIV investigation, AIAA-4202 (2008).
[3] M. L. Post, and T. C. Corke, Separation control using plasma actuators—dynamic stall vortex control on an oscillating airfoil, J. AIAA. 44(2006) 3125–3135.
[4] H. Do, W. Kim, M. O. Mungal, and M. A. Cappelli, Bluff body flow separation control using surface dielectric barrier discharges, AIAA-939 (2007).
[5] F. O. Thomas, A. Kozlov, and T. C. Corke, Plasma actuators for cylinder flow control and noise reduction, J. AIAA 46 (2007) 1921–1931
[6] D. Schatzman, and F. O. Thomas, Turbulent boundary layer separation control using plasma actuators, AIAA-4199 (2008).
[7] J. W. Baughn, C. Porter, B. L. Peterson, T. E. McLaughlin, C. L. Enloe, G. I. Font and C. Baird, Momentum transfer for an aerodynamic plasma actuator with an imposed boundary layer, AIAA-168 (2006).
[8] T. C. Corke, C. He and M. Patel, Plasma flaps and slats: an application of weakly-ionized plasma actuators, AIAA-2127 (2004).
[9] J. Huang, T. C. Corke and F. O. Thomas, Plasma actuators for separation control of low-pressure turbine blades, J. AIAA 44 (2004)51–57.
[10] D. K. Van Ness, T. C. Corke and S. C. Morris, Turbine tip clearance flow control using plasma actuators, AIAA-0021 (2006).
[11] I. Langmuir, Proc Nat Acad Sci 14 (1926).
[12] A. N. M. M. I. Mukut, H. Mizunuma, H. Obara and T. Segawa, Flow characteristics induced by winglet-type plasma actuators, J. Fluid Sc. and Tech. 8 (2013).
[13] Y. B. Suzen, P.G. Huang, J.D. Jacob and D.E. Ashpis, Numerical simulation of plasma based flow control applications, AIAA-4633
[14] M. Forte, J. Jolibois, F. Baudoin, E. Moreau, G. Touchard, M. Cazalens, Optimization of a dielectric barrier discharge actuator by stationary and non-stationary measurements of the induced flow velocity: application to airflow control, Exp Fluids 43:917–928

6th BSME International Conference on Thermal Engineering (ICTE 2014)

Transient Analysis Of 3-Lobe Bearings Considering Surface Roughness Effect For A Gas Turbine

Nabarun Biswas[a]*, Prasun Chakraborti[b]†

[a]*Department of NIT Agartala, Jirania, Tripura-799046, India
[b]Department of NIT Agartala, Jirania, Tripura-799046, India

Abstract

The performance of a 3-lobe bearing is investigated by means of three-dimensional computational fluid dynamics analysis. Surface roughness effects were included in the computation of unsteady transient analysis of 3-lobe bearing, taking into account gravity. Each of the lobes is placed at a distance of 120 degree. In this paper K-Epsilon turbulence model is used. The 3-lobe bearing is designed in Gambit software, the journal is modeled as a ''moving wall'' with an absolute rotational speed of 6000 rpm. Design parameters like L/D ratio, total pressure distribution, surface roughness and lubricant flow properties like turbulent viscosity and velocity magnitude are considered for the analysis The flow is simulated using Ansys Fluent software.

Keywords: 3-lobe; viscosity; pressure; wall shear stress; surface roughness.

1. Introduction

A bearing is a system of machine elements which supports another moving machine element; it permits relative motion while carrying the load. Lubricant applied load for reducing friction between the relatively moving surfaces. As modern science and technology is developing, one discovered that the lubricant is affected by the gap of bearing. The interaction degree between the lubricant and solid surface influences the lubrication property of the bearing clearly. Dr G. Bhushan, Dr S. S. Rattan, Dr N. P. Mehta [5] worked on "Effect of Pressure Dams and Relief-

* Corresponding author. Tel.: +0-000-000-0000 ; fax: +0-000-000-0000 .
  E-mail address: mechanical.biswas@gmail.com

tracks on the Performance of a Four-lobe Bearing" .Their main findings are the following- the presence of pressure dams and relief cracks on the performance of an ordinary four lobe bearing. The generation of pressure and their circumferential variation in the upper half of a bearing primarily affect the stability of a rotor bearing system. In qualitative terms, the proportion of hydrodynamic load generated in upper half with respect to load generated in lower half is one of the deciding factors as to how stable a bearing would be. The magnitude and pressure generated in the lobes of the four-lobe bearing without and with dam indicate that the latter would provide a relatively smoother operation of the bearing. A four-lobe pressure dam bearing operates in the higher range of eccentricity ratios compared to an ordinary four-lobe bearing. There is a marginal increase in the dimensionless friction coefficient when pressure dams are incorporated in an ordinary four-lobe bearing. The stability of an ordinary four-lobe bearing increases when pressure dams and relief-tracks are incorporated in it.

F.A Martin and A.V. Ruddy [6] worked on "The effect of manufacturing tolerances on the stability of profile bore bearings". Their main findings are - the introduction of new quantities of speed independent of the clearance and clearance independent of speed. They gave a more precise analysis to problem than quantities like M' and W' which arise due to various factors and are not independent of machining allowances. The method could be well implemented for 4-lobe bearing. The tighter bearing tolerances results to higher instability at increased condition of speed and turbulence as there is no chance of loss of thermal quantities over them. They categorised the tolerances in two distinct parts like tolerances on the shaft and the tolerances on the bearing itself. Both these clearances play a distinct role in the instability in the bearings caused at very high speeds. The importance of considering the tolerances is based on the fact that tighter tolerances result in the higher instability like vibrations, overheat and wear and tear.

Raghunandana. K. [7] worked on "Inverse Design Methodology for the Stability Design of Elliptical Bearings Operating with Non-Newtonian Lubricants". They considered lubrication as Newtonian in nature which incidentally allowed error in calculation of various critical parameters. This study provided steady state results for different L/D and eccentricity ratios in the form of empirical equations Hence the simulation with the various data and with the aid of computational methods various factors like oil film density and oil film viscosity could be found out for various NON-NEWTONIAN fluids and for BINGHAM plastics too.

J.D Knight and L.E. Barrett [8] worked on "An Approximate Solution Technique for Multilobe Journal Bearings Including Thermal Effects, with Comparison to Experiment". They proposed an approximate solution method for multilobe journal bearings that includes thermal effect. Comparison of solutions obtained by the variable viscosity method to effective viscosity solutions after Lund and Thomsen illustrates discrepancies in operating eccentricity and stiffness coefficients between the two approaches. They also derived a very good co-relation between the variable viscosity solutions and experimental measurements reported by Tonnesen and Hansen of eccentricity, pressures, and temperatures in a two-axial groove bearing.

Nomenclature

C_p	Specific heat(Kg-K)
L/D	Length/Diameter ratio
T	Temperature (^{0}C)
RPM	Revolution per minute
Subscripts	
Avg	Average
Max	Maximum

---

2. Objective

The scope of this work is to design 3 lobe bearing and to analyze the various flow parameters which arise due to the motion of the shaft at rpm of 6000 and surface roughness 0.9 is considered. By using Gambit the design of 3-lobe bearing is done and analysis part is done in FLUENT.

3. Methodology

The main objectives in this stage are:-

- To find the pressure distribution across the various parts of the oil media as well as the shaft in an unsteady condition.
- In this study six time steps 20, 40, 60, 80,100 and 120 seconds are taken and L/D ratio as 0.25,0.5. After 110 seconds the unsteady condition becomes steady. The properties do not change with time after 110 seconds.

4. Equations

The steady, conservative form of Navier-Stokes equations in two dimensional forms for the incompressible flow of a constant viscosity fluid is as follows
Continuity:

$$\frac{\partial U}{\partial X} + \frac{\partial V}{\partial Y} = 0 \tag{1}$$

X- momentum:

$$\frac{\partial(UU)}{\partial X} + \frac{\partial(VU)}{\partial Y} = -\frac{\partial P_n}{\partial X} + \frac{1}{R_e}\left(\frac{\partial^2 U}{\partial X^2} + \frac{\partial^2 U}{\partial Y^2}\right) \tag{2}$$

Y- momentum:

$$\frac{\partial(UV)}{\partial X} + \frac{\partial(VV)}{\partial Y} = -\frac{\partial P_n}{\partial X} + \frac{1}{R_e}\left(\frac{\partial^2 V}{\partial X^2} + \frac{\partial^2 V}{\partial Y^2}\right) \tag{3}$$

Where,

$$X = \frac{x}{D} , Y = \frac{y}{D} , P_n = \frac{p}{\rho u_\infty^2} , U = \frac{u}{u_\infty}, V = \frac{v}{u_\infty}, \ R_e = \frac{\rho u_\infty D}{\mu}$$

In the present study, a three-dimensional numerical study of unsteady, static pressure across the various parts of the oil media as well as the shaft of the 3-lobe bearing is done.

5. Meshing in Gambit (a standard modeling tool)

The part of the oil flooded region is meshed using GAMBIT. The model is exported to fluent for post analysis and results.
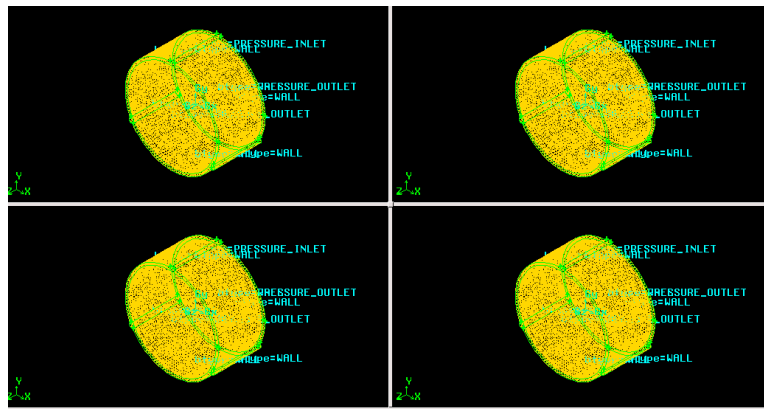

Fig .1. The 4-D view of the meshed part

6. Grid arrangement

The mesh file obtained from the Gambit was exported to Ansys Fluent for subsequent analysis. The mesh file was linked to Fluent and subsequently its grid checking result was surfaced as error free. Eventually it is assumed for formation one default surface at the boundary of the shaft and oil surface.

The rest of the surfaces were defined in the similar manner. The following conditions were assigned to the various components-

Table 1. Defining the various walls and interfaces

Zone	Type
Fluid wall interface	Interior
Fluid	Fluid
Wall 1	Inlet Pressure
Wall 2	Outlet Pressure
Wall 3	Wall

7. Boundary condition for fluid

Physical properties of the fluid (SAE 50) like specific heat, thermal conductivity, viscosity and density were taken as 2270 kg-K, 0.62 W/m-K, 0.044 kg/m-s and 899 kg/m^3 respectively.
Various parameters considered are given below -

Table 2. Defining the boundary conditions for wall

Property	Value
Gauge Total Pressure	101325(Pascal)
Supersonic Pressure	0(Pascal)
Direction Specification Method	Normal to the boundary
Temperature	300(k)

The wall was considered to be stationary with no slip condition and Marangoni stress. The wall thickness was considered to be negligible. The thermal conditions are illustrated below:-

Table 3 . Defining conditions for wall

Property	Value	Nature
Temperature	300(K)	Constant
Heat Generation Rate	0(W/m3)	Constant

Steel was considered as wall material whose properties like density, specific heat and thermal conductivity are taken as 8080 kg/m^3, 509.48 J/kg-K and 11.27 W/m-K respectively.

8. Results and Discussion

The results obtained for a bearing with the following parameters are presented here: L/D ratios are 0.25 and 0.5, radial clearance = 0.05mm, journal speed (n) = 6000 rpm and surface roughness 0.9. The transient variations of oil pressure are studied. In this study six time steps 20, 40, 60, 80,100 and 120 seconds are taken respectively for unsteady analysis. After 120 seconds the unsteady condition becomes steady. It is observed that the properties do

not change much with time after 110 seconds. The results are further iterated for a value of 1000 for convergence criterion of 0.1. The results converged in 441 iterations.
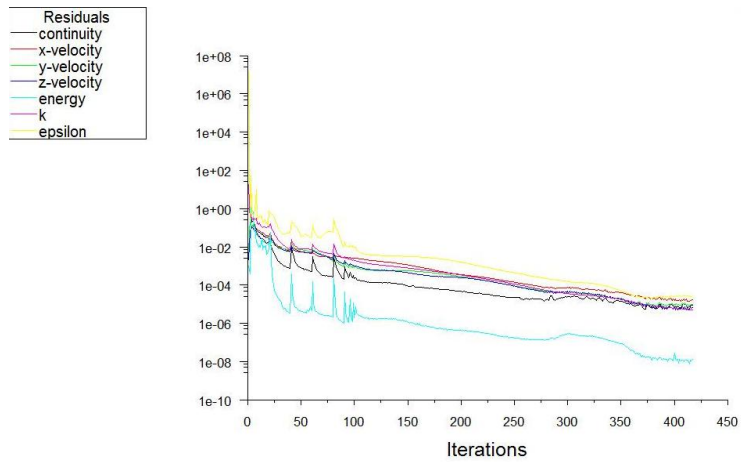

Fig.2. Convergence plot for scaled residuals @ 6000 rpm

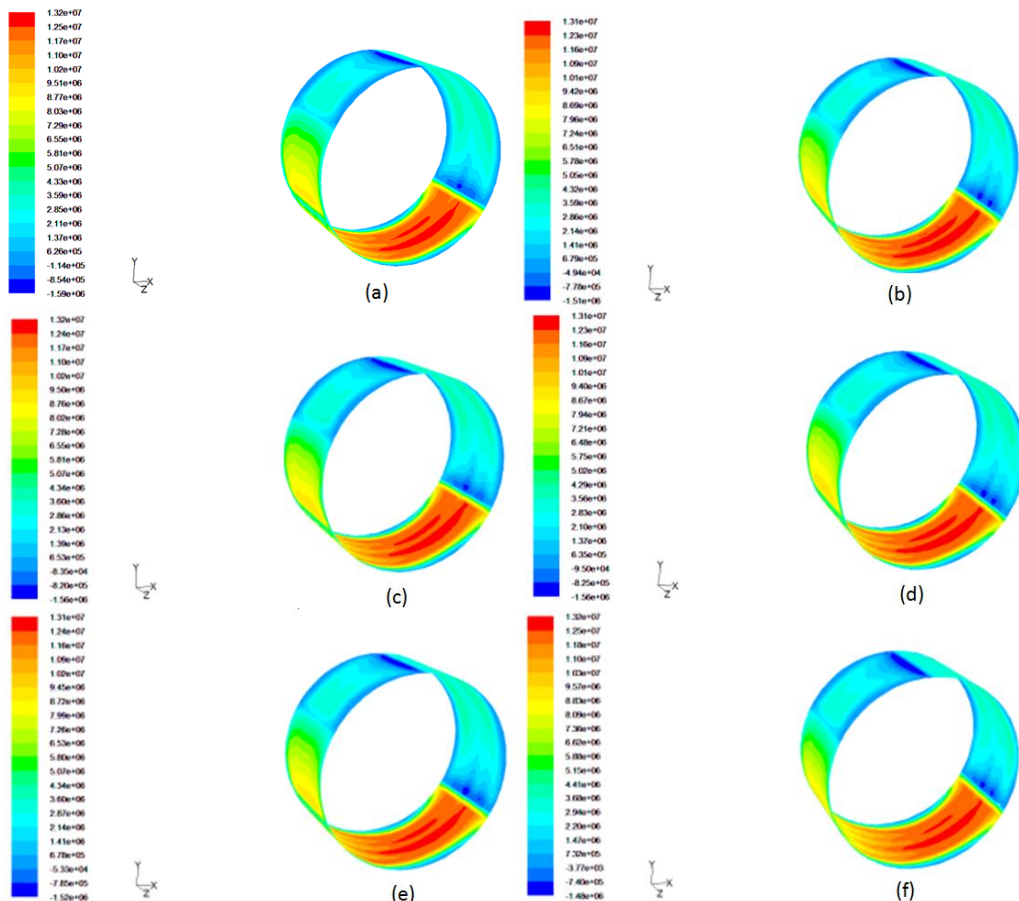*8.1. Fluent analysis of total pressure at 6000 rpm, roughness=0.9 and L/D=0.25*

Fig.3. Contours(a),(b),(c),(d),(e),(f) are total pressure @ 6000 rpm after 20,40,60,80,100 and 120 sec respectively when surface roughness 0.9.

The total pressure predominates near the shaft surface when the surface roughness is 0.9 where the total pressure comes into picture due to rotation of the shaft. For rotation of the shaft in 6000 rpm the maximum total pressure distribution is same. The value is 1.32e+07pascal.

8.2. Fluent analysis for total pressure at 6000 rpm, roughness=0.9 and L/D=0.5
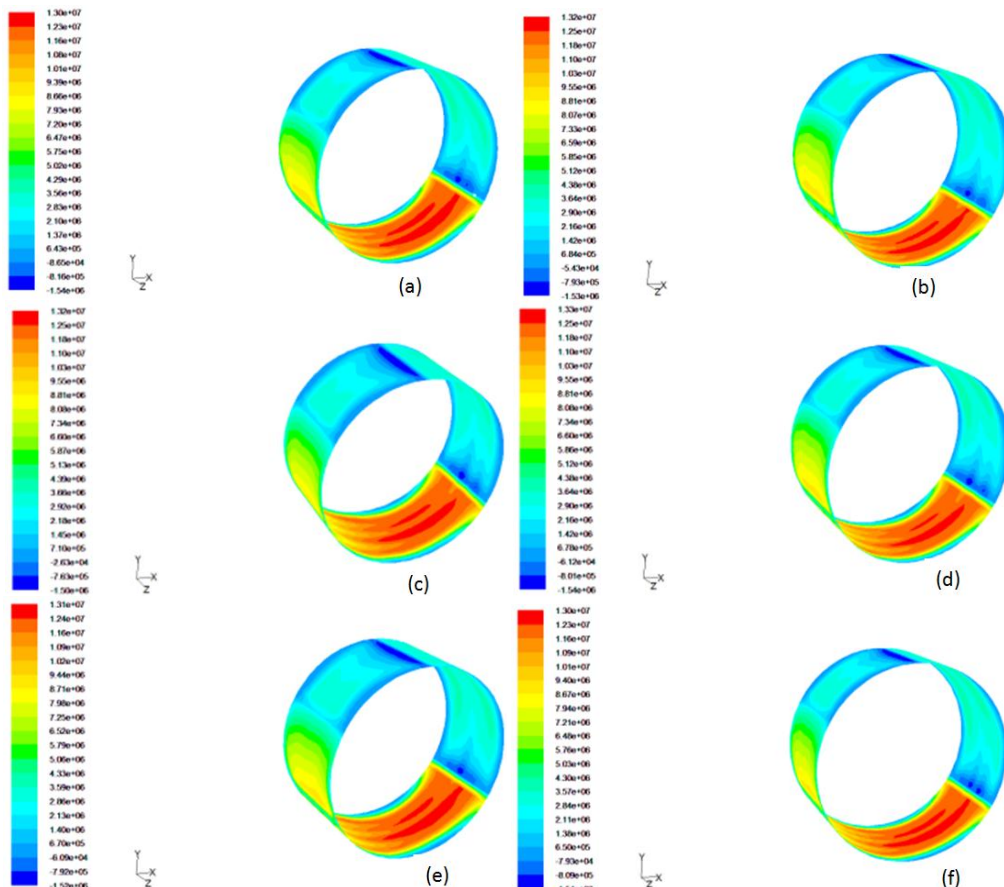

Fig.4. Contours(a),(b),(c),(d),(e),(f) are total pressure @ 6000 rpm after 20,40,60,80,100 and 120 sec respectively when surface roughness 0.9.

When the surface roughness is 0.9 then total pressures also predominates near the shaft surface due to rotation of the shaft. For rotation of the shaft in 6000 rpm the maximum total pressure distribution is same. The value is 1.30e+07pascal.

9. Conclusion

The contours of the bearing exhibit distinct pattern to surface critical values of pressure near the interface of the wall and the surface of the shaft. It is observed after 441 iterations the critical pressure gets stabilized. Transient dynamic behavior of thin film lubricated journal bearing system is studied and presented. From pressure plots, it is observed that the maximum pressure, the bearing can withstand is increasing with increase in roughness value. The maximum pressure is noted at minimum oil film thickness. Transient dynamic behavior of thin film lubricated journal bearing system have been studied and presented. From pressure plots, it is observed that the total pressure increases when roughness increases.

References

[1] Dr G. Bhushan, Dr S.S. Rattan, Dr N P Mehta, Effect of Pressure Dams and Relief-tracks on the Performance of a Four-lobe Bearing, IE (I) Journal MC (2005) 194-198.
[2] F.A Martin and A.V. Ruddy, The effect of manufacturing tolerances on the stability of profile bore bearings, (1984) 494-499.
[3] Raghunandana. K., Inverse Design Methodology for the Stability Design of Elliptical Bearings Operating with Non-Newtonian Lubricants, World Congress on Engineering and Computer Science, October 24-26, 2007
[4] J.D Knight, L.E. Barrett, An Approximate Solution Technique for Multilobe Journal Bearings Including Thermal Effects, with Comparison to Experiment, 26(4) (1983) 501-508.
 [5] A. Radfordand D. Fitzgeorge, The effects of journal lobing on the performance a hydrodynamic plain journal bearing wear, 45(3) (1977) 311-322.
[6] S. Basri and D.T. Gethin, A comparative study of the thermal behaviour of profile bore bearings, Tribology International, 23(4) (1990) 265-276.
[7] T. S. R. Murthy, Y. Balaramaiah, V. C. Venkatesh, An Analysis of a Special Hydrodynamic Bearing for Machine Tool Spindles, CIRP Annals - Manufacturing Technology, 32(1) (1983) 319-325.
[8] F. Al-Bender, K. Smets, Development of Externally Pressurised Foil bearings", Tribology and Interface Engineering Series, 49 (2006) 345-401.
[9] A. Kumar, S. S. Mishra, Steady state analysis of noncircular worn journal bearings in non laminar lubrication regimes, Tribology International, 29(6) (1996) 493-498.
[10] U. Singh, L. Roy, and M. Sahu, Steady-state thermo-hydrodynamic analysis of cylindrical fluid film journal bearing with an axial groove, Tribology International, (2003) 625-632.
[11] S. Basri, D.T. Gethin, Axially profiled circular bearings and their potential application in high speed lubrication,Wear, 146(1,30) (1991) 125-135.
[12] L. Roy, Steady state thermo-hydrodynamic analysis and its comparison at five different feeding locations of an axial grooved oil journal bearing is obtained theoretically", Tribology International, 42(8) (2009) 1187-1198.
[13] J. D. Knight, L. E. Barrett , An Approximate Solution Technique for Multilobe Journal Bearings Including Thermal Effects, with Comparison to Experiment, Tribology Transactions, 26 (4) (1983) 501-508.
[14] Stanisław Strzelecki, Sobhy M. Ghonheam, Dynamically loaded cylindrical journal bearing with recess" Journal of Kones International Combustion engines 11(3-4) (2004)
[15] Sobhy M. Ghoneam, Stanisław Strzelecki, Thermal problems of multilobe journal bearing tribosystem, Meccanica , 27 February 2006
[16] Edmund A. Memmott, Oscar De Santiago, A classical sleeve bearing instability in an overhung compressor, CMVA, 2007
[17] Dr G. Bhushan, Dr S.S Rattan, Dr N.P. Mehta, Effect of Pressure Dams and Relief-tracks on the Performance of a Four-lobe Bearing, IE (I) Journal MC (2005) 194-198
[18] F.A Martin, A.V. Ruddy, The effect of manufacturing tolerances on the stability of profile bore bearings, (1984) 494-499.

6th BSME International Conference on Thermal Engineering (ICTE 2014)

Experimental investigation on the performance of NACA 4412 aerofoil with curved leading edge planform

M. Nazmul Haque[a*], Mohammad Ali[a] , Ismat Ara[a]

[a]*Department of Mechanical Engineering, Bangladesh University of Engineering and Technology, Dhaka-1000, Bangladesh.*

Abstract

Aircraft wings are the lifting surfaces with the chosen aerofoil sections. The efficiency as well as the performance of an aircraft mostly depends on the aerodynamic characteristics e.g. lift, drag, lift to drag ratio, etc of wings. Besides many factors, the effects of wing shape are also crucial to aircraft performance. This paper represents the experimental investigation to explore better aerodynamic performance by incorporating curvature at the leading edge of a wing. A wooden model with straight leading and trailing edge i.e. rectangular planform and another model with curved leading edge and straight trailing edge are prepared with NACA 4412 aerofoil in equal length (span) and surface area. Both the models are tested in a closed circuit wind tunnel at air speed of 85.35 kph (0.07 Mach) i.e. at Reynold's number 1.82 x 10^5. The static pressure at different angles of attack (-4$^°$, 0$^°$, 4$^°$, 8$^°$, 12$^°$, 16$^°$, 20$^°$ & 24$^°$) are measured from both upper and lower surfaces of the wing models through different pressure tapings by using a multi-tube water manometer. From the static pressure distribution, lift coefficient, drag coefficient and lift to drag ratio of both the models are analyzed. After analyzing the data, it is found that the curved leading edge wing planform is having higher lift coefficient and lower drag coefficient than the rectangular wing planform. Thus, the curved leading edge planform is having higher lift to drag ratio than the rectangular planform.

Keywords: Aerofoil; aerodynamic performance ; coefficient of lift; coefficient of drag; lift to drag ratio; Reynold's number.

* Corresponding author. Tel.: +88-01784660933.
  E-mail address: nazmul_me@hotmail.com

1. Introduction

Similar to a bird's wing, an aircraft wing is the lifting surface with the chosen aerofoil section, whose shape/geometry can be varied span wise to search better performance. The lift generated by the wing sustains the weight of the aircraft to make flight in the air. Again, from an aerodynamic perspective, the main source of the airplane drag is associated with the wing. Around two-thirds of the total drag of typical transport aircraft at cruise conditions is produced by the wing [1]. Therefore, the effects of wing shape and size are crucial to aerodynamic characteristics (lift, drag, lift to drag ratio, etc) on which the efficiency as well as the performance of aircraft depend. As such, researches on different wing shapes/geometries are still on throughout the world to explore the maximum possible lift and minimum possible drag. Hossain et al. [2] conducted an experimental analysis for the aerodynamic characteristics of rectangular wing with and without bird feather like winglets for different Reynolds Number. The experimental result shows 25~30% reduction in drag coefficient and 10~20% increase in lift coefficient by using bird feather like winglet at 8 degree angle of attack. Dwivedi et al. [3] adopted a simple approach for experiment on aerodynamic static stability analysis of different types of wing shapes. They tested the reduced scale size wings of different shapes like rectangular, rectangular with curved tip, tapered, tapered with curved tip, etc. in low speed subsonic wind tunnel at different air speeds and different angles of attack. The authors found that the tapered wing with curved tip was the most stable at different speeds and ranges of working angles of attack. Mineck et al. [4] tested three planar, untwisted wings with the same elliptical chord but with different curvatures of the quarter-chord line. They found that the elliptical wing with the unswept quarter-chord line has the lowest lifting efficiency, the elliptical wing with the unswept trailing edge has the highest lifting efficiency and the crescent-shaped wing has efficiency in between. Recktenwald [5] tested a circular planform non-spinning body with an airfoil section configuration developed and produced by Geobat Flying Saucer Aviation Inc. in the Auburn University wind tunnel facility. For comparison purpose, a Cessna 172 model was also tested. The author found that the lift curve slope of the Geobat was less than that of Cessna 172 but displayed better stall characteristics. Wakayama [6] studied and presented basic results from wing planform optimization for minimum drag with constraints on structural weight and maximum lift. Moreover, aerodynamic characteristics analysis for different airfoils have also been conducted at different corners of the world like Mahmud [7] analyzed the effectiveness of an airfoil with bi-camber surface, Kandwal et al. [8] studied the fluid flow and aerodynamic forces on an airfoil, Robert [9] studied the variation of pressure distribution over an airfoil with Reynold's Number, Sharma [10] analyzed the flow behavior around an airfoil body, etc.

Researches on different airfoils and conventional wing geometries like rectangular, sweepback, tapered or, delta shapes have been carried out in many places around the world in an extensive way. But aerodynamic characteristics of curved-edge wing geometries are yet to be explored. As such, the proposed experimental investigation is carried out in the wind tunnel to explore aerodynamic characteristics of curved leading edge wing. Similar characteristics of a rectangular wing of equal span and surface area are also investigated in the same way for reference. At the end, the characteristics of the curved leading edge wing are compared with that of the rectangular wing.

Nomenclature

α	Angle of attack (AOA)
C	Chord length
S	Span
C_L	Coefficient of lift
C_D	Coefficient of drag
L/D	Lift to drag ratio
R_N	Reynold's number
U_∞	Free stream velocity of air in the wind tunnel
P_∞	Free stream pressure

2. Design and construction

The aerodynamic characteristics (C_L, C_D and L/D) can be calculated from the surface pressure distribution of the wing [11]. To obtain the pressure distribution over the surfaces, wooden wing models are prepared with a specific aerofoil, suitable fixture is prepared to set the models in the wind tunnel and a multi-tube manometer is fabricated to take the pressure readings from the surfaces of the wing models.

2.1. Wing models

Using NACA 4412 aerofoil, wooden models for rectangular wing and curved leading edge wing are prepared having the same span (245 mm) and equal surface area (31115 mm^2). Each model is provided with 32 pressure tapings along the span and chord (16 at upper surface & 16 at lower surface). Along the span the wings are divided into 4 equal segments (61.25 mm). For rectangular wing, the chord length is same (127 mm) for all the four segments but for the curved leading edge wing, the average chord length is different for different segments along the span (for segment A- 152.4 mm, for segment B- 140 mm, for segment C- 110 mm and for segment D- 101.6 mm). 4 pressure tapping points at upper surface and 4 pressure tapping points at lower surface are made at 20%, 40%, 60% and 80% of the average chord length of each segment of both the wings as shown in Fig. 1. The multi-tube manometer mainly consists of a water tank and 36 manometer glass tubes connected to the tapping points in wing model surfaces. The water tank is used to store the distilled water. Each limb is fitted with a scale graduated in mm to measure the difference of water height. The static pressure is calculated from the difference in water height.
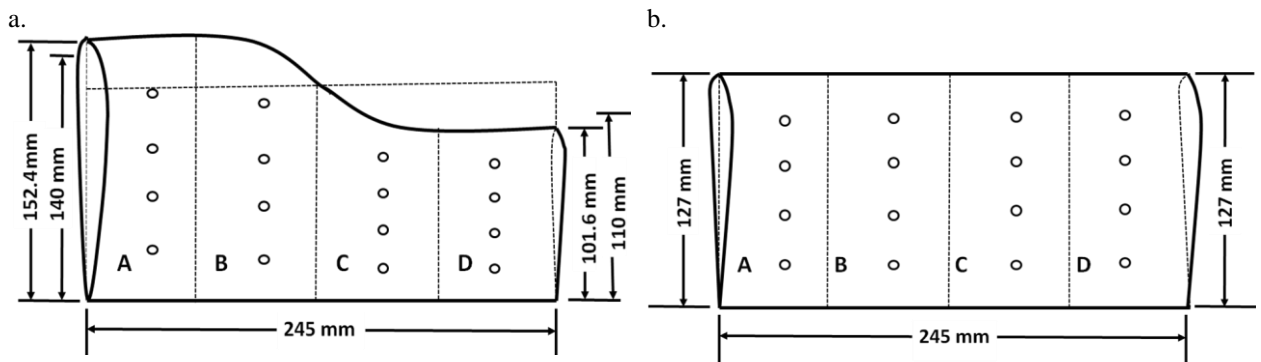

Fig.1. (a) Curved Leading Edge Planform (b) Rectangular Planform

2.2. Fixture for altering AOA

A fixture is fabricated and fixed in the test section of the wind tunnel as shown in Fig. 2. The fixture facilitates the wing models to rotate and fix at any angle of attack. The wing models are tested at AOA from -4˚ to 24˚ with a step of 4˚. Each model is rotated and fixed at the desired angle by seeing the preset scales (in degrees) pasted on the frame.

3. Experimental method

3.1. Experimental setup

The experiment is carried out in a 700mm×700mm closed circuit wind tunnel as shown in Fig. 2 available at turbulence laboratory of Department of Mechanical Engineering, BUET. The wind speed is created by the two 700mm counter rotating fans. At the discharge of the fans there is a silencer to reduce the sound level. From the silencer air flow passes through the flow controlling butterfly valve, diffuser and the plenum chamber to stabilize the

flow to certain level. The fan motors are powered by 400V-3Φ-50Hz power supply through motor speed controller. Thus the wind speed in the tunnel can be varied both by controlling the fan motor speed as well as by controlling the butterfly valve. To facilitate the present experiment in the open air condition the diffuser at the end of the test section is taken out and the discharge side of the test section is fitted with a 700mm×700mm discharge duct and a 1000mm×1000mm to 762mm×762mm bell mouth entry is added at the return duct to have smooth entry. Thus the 406 mm open flow field created between the discharge duct and bell mouth entry become the experimental space where desire velocity is obtained.
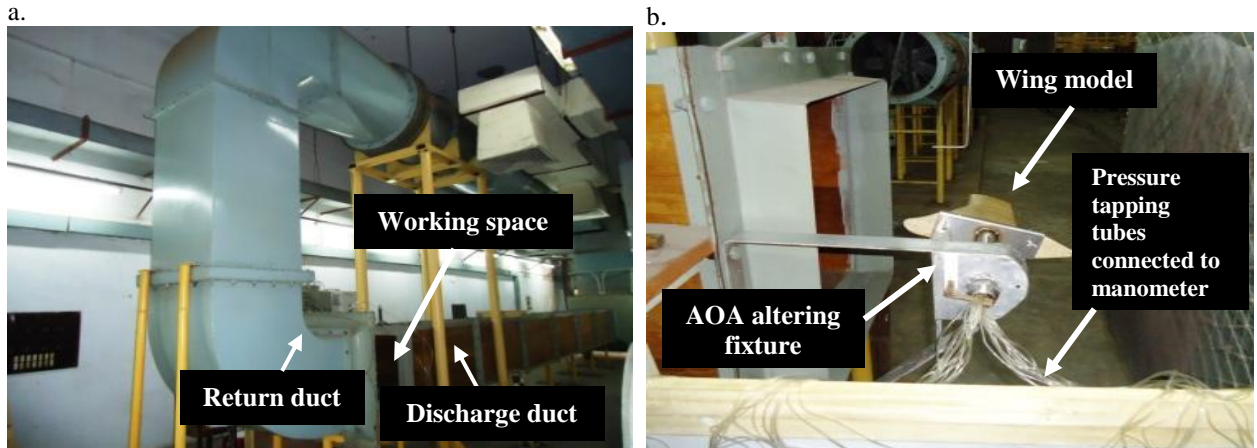
a.

b.

Fig. 2. (a) Wind tunnel at BUET's Turbulence laboratory (b) Experimental set-up

3.2. Test conditions and procedures

All the experimental data were taken at room temperature of 35˚C and at air speed of 23.71 m/s (85.35 kph) and the air flow was considered incompressible throughout the experiment. The static pressure at different AOA (-4˚, 0˚, 4˚, 8˚, 12˚, 16˚, 20˚ & 24˚) are measured from both upper and lower surfaces of the wing models through different pressure tapings by using a multi-tube water manometer. Specific density of both air and water corresponding to room temperature was assumed to be 1.145 kg/m^3 and 994 kg/m^3 respectively.

4. Mathematical modeling

Surface pressure coefficient, C_p can be calculated from the static pressure by the following formula [12].

$$c_{p,i} = \frac{p_i - p_\infty}{\frac{1}{2}\rho U_\infty^2} \tag{1}$$

Where, P_i is the surface static pressure. Values of C_p at any point over the aerofoil surface can be approximated from the corresponding boundary values by using the first order Lagrange interpolation and extrapolation:

$$c_p(x) = \frac{(x - x_1)}{(x_0 - x_1)}c_{p,o} + \frac{(x - x_0)}{(x_1 - x_0)}c_{p,1} \tag{2}$$

An integration of a pressure distribution over an airfoil chord for both upper and lower surfaces is known to provide normal and axial force acting on an airfoil section when shear stress due to viscous effect is neglected [11, 13].
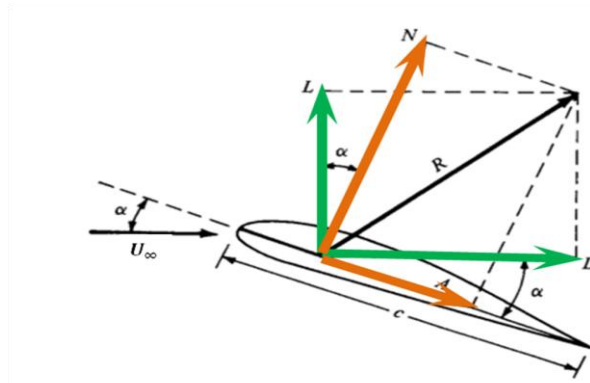

Fig. 3. Diagram of resultant aerodynamic force and its components acting on a wing section

With x as a chordwise direction and y as a perpendicular one, both normal and axial force integral equations are given respectively as:

$$C_n = \frac{1}{c}\int_0^c (c_{p,l} - c_{p,u})dx \qquad (3)$$

$$C_a = \frac{1}{c}\int_0^c (c_{p,u}\frac{dy_u}{dx} - c_{p,l}\frac{dy_l}{dx})dx \qquad (4)$$

When the notation l is for the lower surface and u is for the upper surface. The known pressure coefficients from the experiment can be calculated for the normal and axial force by using a numerical integration of the above equations in the Trapezoidal approximating forms. Both surfaces are divided into small panels corresponding to a total of gaps between each pressure tap location. When n is a number of panels, the equations can be converted to:

$$C_n = \sum_{i=1}^n \left[\left(c_{p,l,i} - c_{p,u,i} \right)\Delta\left(\frac{x_i}{c}\right) \right] \qquad (5)$$

$$C_a = \sum_{i=1}^n \left[\left(c_{p,u,i}\frac{\Delta y_{u,i}}{\Delta x_i} - c_{p,l,i}\frac{\Delta y_{l,i}}{\Delta x_i} \right)\Delta\left(\frac{x_i}{c}\right) \right] \qquad (6)$$

The interpolated and extrapolated pressure coefficients would be applied to Equation (5) and (6) in order to get the normal and axial force at a section of interest. Lift and drag coefficient can be obtained from:

$$c_l = c_n Cos\alpha - c_a Sin\alpha \qquad (7)$$

$$c_d = c_n Sin\alpha + c_a Cos\alpha \qquad (8)$$

The over-all value of the coefficients for the whole wing can be found out by averaging the same values of each segments of the wing along the span.

5. Results and discussions

5.1. Surface pressure distribution

Pressure coefficient for each tapping point (at 20%, 40%, 60% & 80% of chord) is determined from the measured surface static pressure and the pressure coefficient of the intermediate points (at 10%, 30%, 50%, 70% & 90% of chord) are approximated through linear interpolation/extrapolation from the measured boundary values. In Fig. 4, distribution of surface pressure coefficient at 0° AOA is shown for each of the four segments of both the rectangular and the curved leading edge wing. Similarly, in Fig. 5, distribution of surface pressure coefficient at 12° AOA is shown. From both the figures it is observed that the difference between the upper and lower surface pressure coefficients at 12° AOA is higher than those at 0° AOA. From Fig. 4, it is observed that the difference between upper and lower surface pressure coefficient near the root of the wing (i.e. at segment A) is lower for the curved leading edge wing than that of the rectangular wing. But near the tip of the wing (i.e. at segment D), the said difference is almost equal. However, at the middle of the wing (segment B & C), the difference is higher for the curved leading edge wing than the rectangular wing. In Fig. 5, at 12° AOA, the difference between upper and lower surface pressure coefficient in the first two segments from the root (segment A & B) is lower for the curved leading edge planform than that of the rectangular planform. But for the next two segments towards the tip of the wing (segment C & D), the difference is relatively higher for the curved leading edge planform.
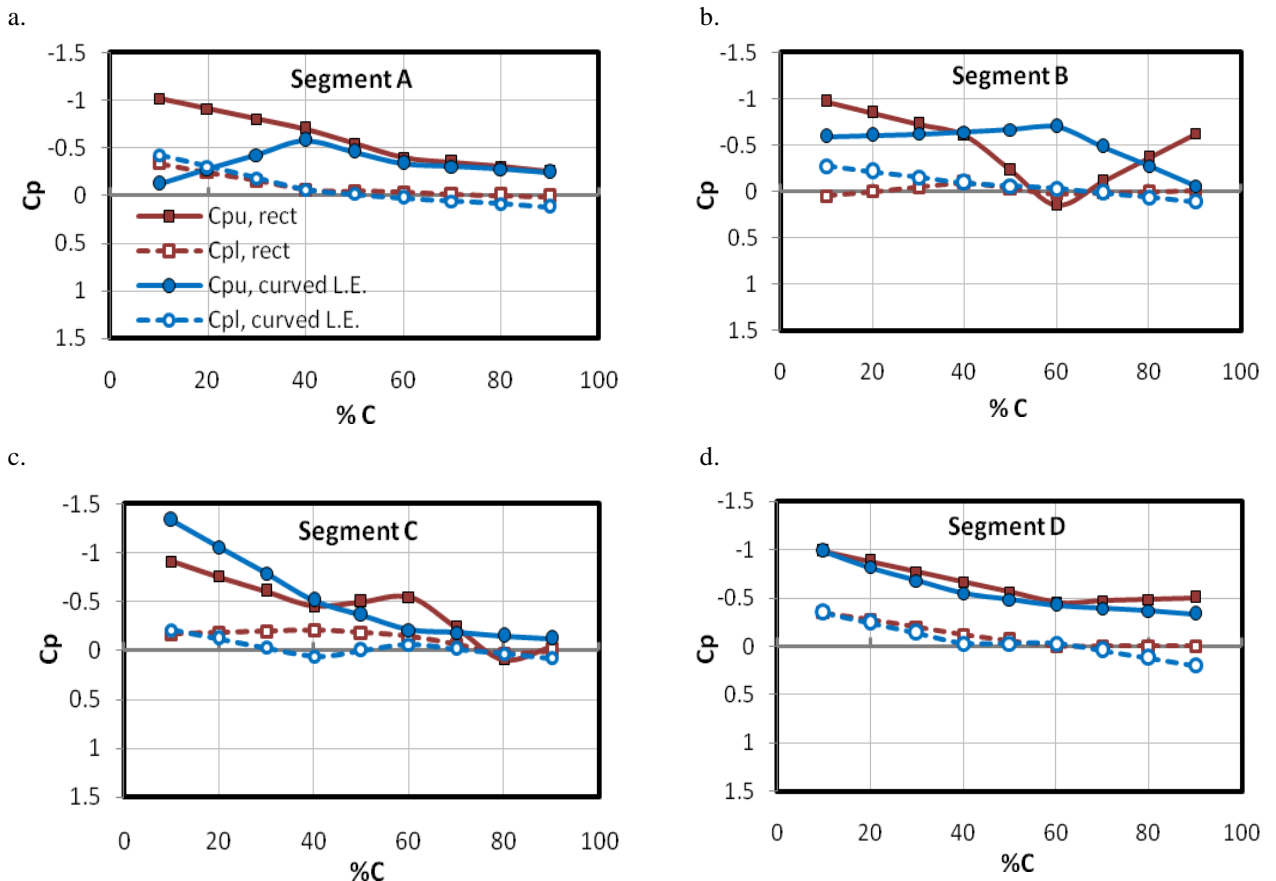
a.

b.

c.

d.

Fig. 4. Surface C_p distribution of different segments of both the wings at α=0°

a.

b.

c.

d.

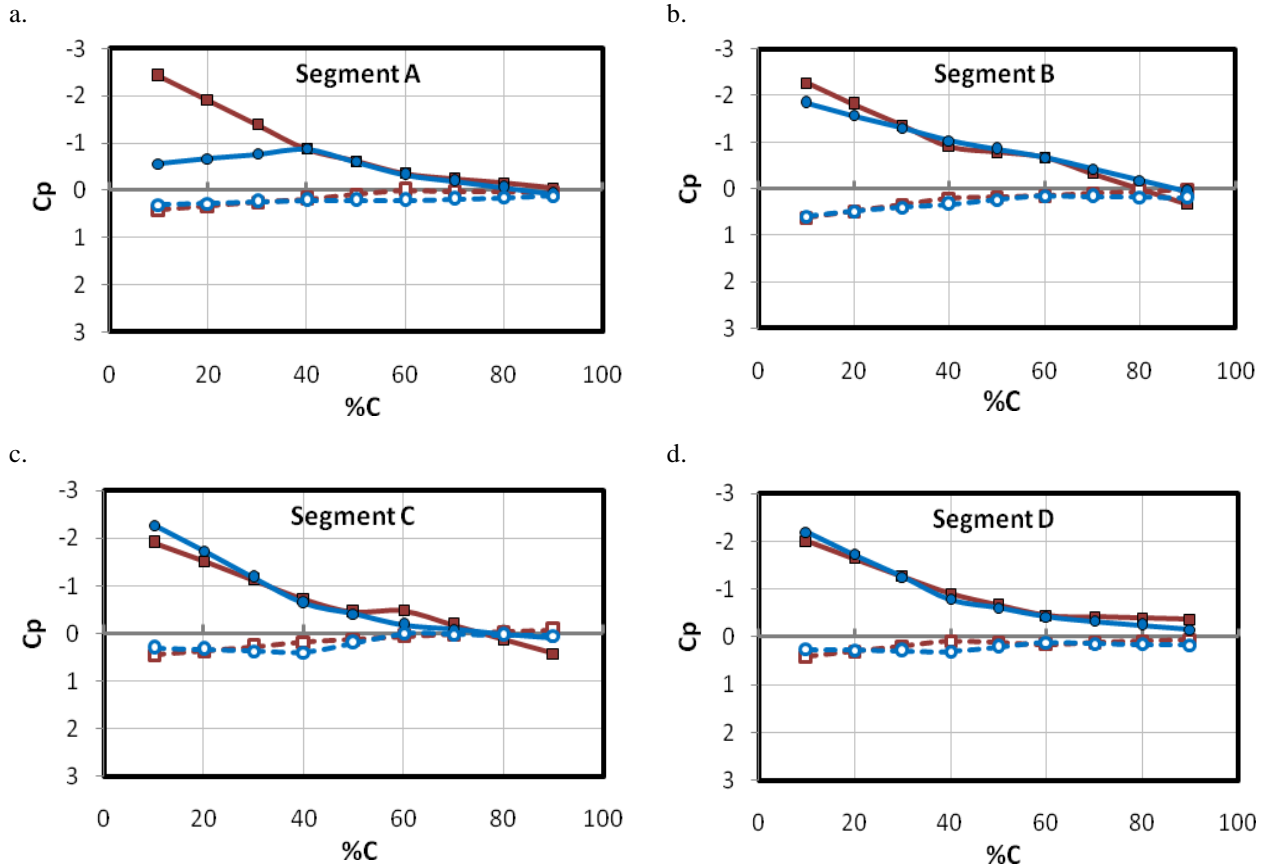Fig. 5. Surface C_p distribution of different segments of both the wings at α=12˚

5.2. Lift characteristics

Variation of lift coefficient at different angle of attack for both the wings is shown in Fig. 6. It is observed that the lift coefficient for curved leading edge wing is higher than the lift coefficient of rectangular wing at every angle of attack. However, greater values of lift coefficient are observed at -4˚, 0˚ and 8˚ angle of attack. Critical angle of attack for both the wings remains within the same range of 12˚~16˚.
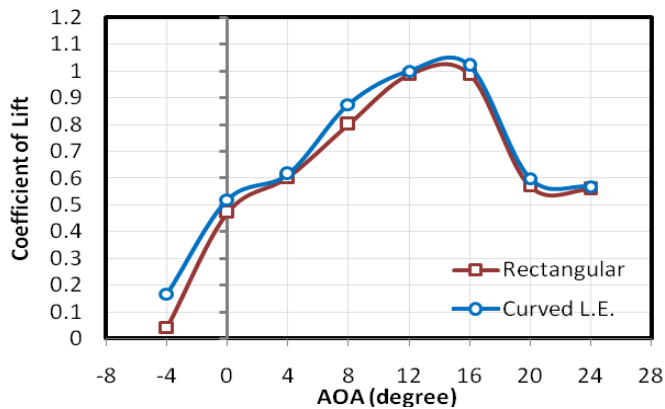

Fig. 6. Variation of lift coefficient with AOA

5.3. Drag characteristics

In Fig. 7, the variation of drag coefficient for both the wings are plotted against different angles of attack and it is observed that the values of drag coefficient for curved leading edge wing is lower than that of the rectangular wing. Prominent reduction in drag coefficient values for curved leading edge wing is found at -4˚ and 12˚ angle of attack.
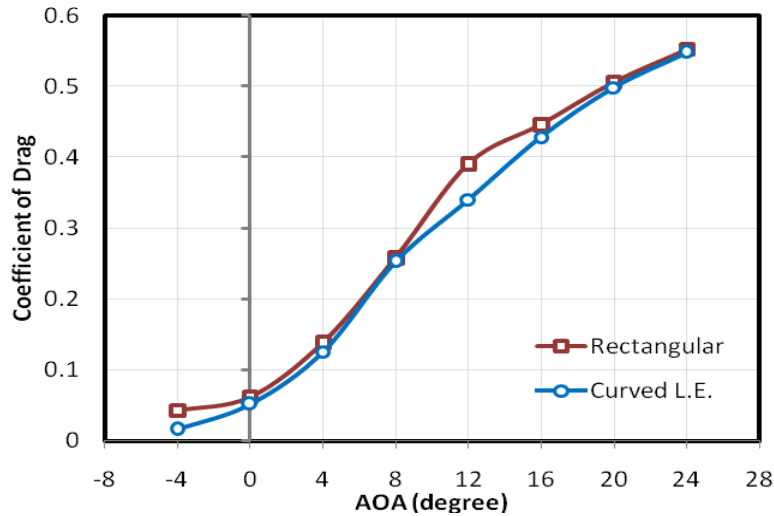
Fig. 7. Variation of drag coefficient with AOA

5.4. Lift to drag ratio

The values of lift to drag ratio are plotted for various angles of attack in Fig. 8 and it shows that the lift to drag ratio of curved leading edge wing is higher than that of the rectangular wing. It is also observed that curved leading edge planform can provide higher lift to drag ratio than the rectangular planform at angles of attack below 12˚.
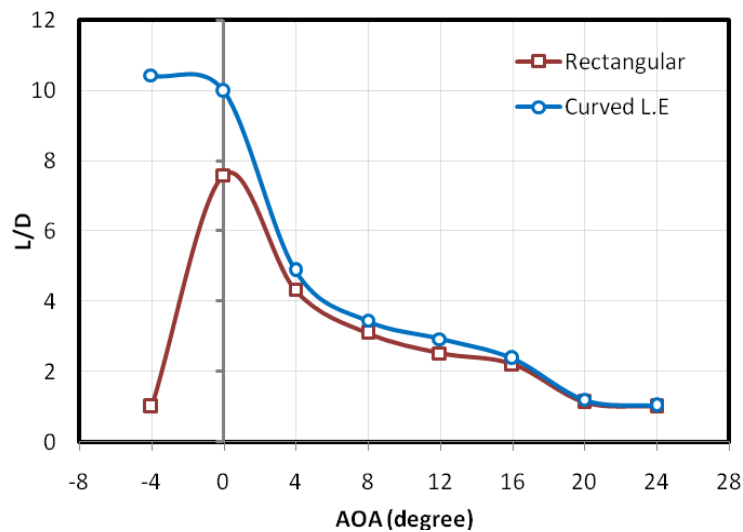
Fig. 8. Variation of lift to drag ratio with AOA

6. Conclusion

In this experiment, curvature is incorporated at the leading edge in such a way that the surface area from the middle of the wing towards the root increases and towards the tip the area decreases in the same rate. The overall surface area of the wing remains same as of the rectangular planform. As a result, the wing can produce more lift due to increased surface area near the root. At the same time, flow separation along the span of the wing is reduced due to gradual reduction of chord length along the span and so the drag is also reduced. From the analysis of experimental data it is observed that the lift coefficient of the curved leading edge planform increases and the drag coefficient decreases at angles of attack below 12˚ in comparison to the rectangular planform; whereas critical angle of attack does not vary significantly between the two planforms. Beyond critical angle of attack, values of lift and drag coefficients are almost equal. As such, it can be concluded that the curved leading edge planform exhibits better aerodynamic performance than the rectangular planform due to higher lift to drag ratio at angles of attack below the critical angle of attack.

Acknowledgements

References

[1]   Lynch, F.T., "Commercial Transports-Aerodynamic Design for Cruise Performance Efficiency," Chapter II in Transonic Aerodynamics, David Nixon, Ed., Progress in Astronautics and Aeronautics, Vol. 81, AIAA, New York, 1982, pp. 81-144.

[2]   Hossain, A., Rahman, A., Iqbal, A.K.M.P., Ariffin, M., and Mazian, M., "Drag Analysis of an Aircraft Wing Model with and without Bird Feather like Winglet", International Journal of Aerospace and Mechanical Engineering, Vol. 6, No.1, 2012, pp.8-13.

[3]   Dwivedi, Y.D., Prasad, M.S., and Dwivedi, S., "Experimental Aerodynamic Static Stability Analysis of Different Wing Planforms", International Journal of Advancements in Research & Technology, Vol. 2, No. 6, June 2013, pp.60-63.

[4]   Mineck, R.E., and Vijgen, P.M.H.W., "Wind-Tunnel Investigation of Aerodynamic Efficiency of Three Planar Elliptical Wings with Curvature of Quarter-Chord Line", NASA Technical Paper 3359, October 1993, pp. 1-20.

[5]   Recktenwald, B., "Aerodynamics of a Circular Planform Aircraft", American Institute of Aeronautics and Astronautics 022308, 2008, pp.1-7.

[6]   Wakayama, S., "Subsonic Wing Planform Design Using Multidisciplinary Optimization", Journal of Aircraft, Vol. 32, No. 4, July-August 1995, pp. 746-753.

[7]   Mahmud, M.S., "Analysis of Effectiveness of an Airfoil with Bi-camber Surface", International Journal of Engineering and Technology, Vol. 3, No. 5, May 2013, pp.569-577.

[8]   Kandwal, S., and Singh, S., "Computational Fluid Dynamics Study of Fluid Flow and Aerodynamic Forces on an Airfoil", International Journal of Engineering and Technology, Vol. 1, No. 7, September 2012, pp.1-8.

[9]   Robert, M.P., "The Variation with Reynolds Number of Pressure Distribution over an Airfoil Section", NACA Report No. 613, pp.65-84.

[10] Sharma, A., "Evaluation of Flow Behavior around an Airfoil Body", M. Engg thesis, Department of Mechanical Engineering, Thapar University, Patiala-147004, India, July 2012, pp.1-60.

[11] Anderson, J.D., "Fundamentals of Aerodynamics", McGraw-Hill Series in Aeronautical and Aerospace Engineering, 3rd Edition, pp. 15-22.

[12] White, F.M., "Fluid Mechanics", McGraw-Hill Series in Mechanical Engineering, 4th Edition, 1999, pp. 526.

[13] Devenport, W.J. and Schetz, J. A., "The Investigation of an Inboard-Winglet Application to a Roadable Aircraft", M Sc in Aerospace Engineering Thesis, Virginia Polytechnic Institute and State University, May 2002, pp. 24-26.

6th BSME International Conference on Thermal Engineering (ICTE 2014)

Experimental Study of Unsteady Flow in a Shock Tube for Needle-Free Drug Delivery

Guang Zhang[1], Yun Sung Kim[2], Gyu Wan Kim[3], Toshiaki Setoguchi[4] and Heuy Dong Kim[1,2,3*]

1. 2. 3. Department of Mechanical Engineering, Andong National University, Andong 760-749, Korea

Zhang1@anuis.andong.ac.kr[1], kimhd@andong.ac.kr[1*]

4. Department of Mechanical Engineering, Saga University, Saga, Japan

setoguci@me.saga-u.ac.jp

Abstract

Recently, the needle-free delivery system has been widely used in medical fields due to its convenience in delivering drug particles into human body without any external needles. In order to penetrate through the outer layer of the skin, drug particles need to obtain enough momentum, which is achieved by accelerating drug particles in a Contoured Shock Tube (CST). The CST consists of a micro shock tube with two diaphragms and an expanded supersonic nozzle. In the present study, experimental studies were carried out by pressure measurement. Six high sensitive pressure transducers were used for recording pressure changes as the shock wave moved through different locations along walls in the test section. From which, data on shock wave propagation could be obtained. Different diaphragm pressure ratios were conducted to demonstrate effects of initial diaphragm pressure ratios on shock wave propagation. Shilieren visualization was also performed to observe shock wave propagation and shock wave structure in the present experimental shock tube model. The characteristic of the internal flow and shock wave system have been studied and analyzed in details in the present shock tube model.

Keywords: Shock tube, Supersonic nozzle, Needle-Free drug delivery, Shock wave propagation, Unsteady flow.

*Corresponding author: Heuy Dong Kim. E-mail address: kimhd@andong.ac.kr
Department of Mechanical Engineering, Andong National University, Korea

1. Introduction

Injecting drugs to human body is an important part in medical science. A unique drug delivery system named as the transdermal drug delivery system has been developed to deliver drug particles to the body without any external needles. Compared to traditional plastic syringes containing some potential danger, prominent advantages are taken by the needle-free drug delivery. Patients suffer less pain and injure free, and no sharp needle is exposed for contamination hazard. As drug particles are delivered by powder form, there is no need to transform them into liquid form any more. This makes storage and transportation much easier and less cost. The delivering process is also very easy and there is no need of any skilled operators. In order to get the optimum effect of the delivered drug, it is very important to deliver it into the desired layer of the skin. It is possible to do that by controlling the momentum of drug particles. Particles are accelerated by high speed gas before being penetrated into the outer layer of the skin. This can be done by using a Contoured Shock Tube (CST). Needle-free drug delivery systems also offer exciting prospect for some unique treatments like DNA vaccination and anti-viral drug delivery which are difficult to execute with the conventional technology. The schematic of needle–free drug delivery system is shown in Fig. 1.
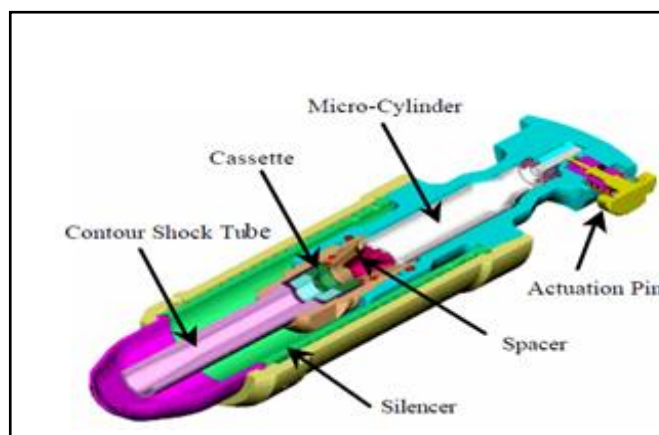

Fig. 1. Schematic of needle-free drug delivery system

The initial work on transdermal drug delivery system was done by M. A. F. Kendall et al who designed a system to deliver DNA coated metal particles into plant cells for genetic modification [1]. They performed an experimental investigation of the transient gas and particle dynamics within a transonic converging-diverging nozzle prototype. Pitot and static pressure measurements, schlieren visualisation and Doppler global velocimetry technique were used to observe the unsteady flow in the converging-diverging nozzle. Results showed that total pressure loss and large nozzle area ratio lead to gas and particle flow non-uniformities generated by oblique shock waves. M. A. F. Kendall [2] also operated experimental study and CFD simulation on a CST model. The CST system delivered particles with a narrow and controlled velocity range and a uniform spatial distribution. Results indicated that the entrained particle payload did indeed achieve a uniform velocity (±4%) at the device exit, which had a good agreement with conclusion from CFD code.

Y. Liu [3-5] et al made numerical simulations on shock wave propagation and interaction between the gas and micro particles in different CST models. Simulations were performed at different drag correlations applied to predict the micro particles transport in numerically simulated gas flow. Simulated pressure histories agreed well with the corresponding Pitot and static pressure measurement. In addition, the calculated velocity distributions also showed good agreement with the best prediction from Igra&Takayama correlation with maximum discrepancy of 5%. M. C. Marrion [6] et al operated static pressure measurements compared to CFD results. Experimental results in the ideal

driver had good agreement with both CFD and one-dimensional analysis. In the obstructed driver, there are strong deviations between experimental results and theoretical analysis, but not in the driven section where pressure measurements matched theory well.

N. J. Quinlan [7] et al conducted an experimental study in the Mach 3.5 contoured nozzle. A numerical model of the quasi-steady flow of stored gas from the reservoir system was introduced. The prediction showed good agreement with measurement of the decaying pressure in the cylinder and rupture chamber at the earliest stages, when the rupture chamber acts as the driver section of a shock tube. The relatively high velocities observed for the smallest particles were due to the use of helium, with its high speed of sound. However, the larger particles tested did not attain such high velocities. R. F. Chisnell [8] took a first-order relationship between changes in area and shock strength which was derived for the case of a shock moving through a channel with a small area change. By suitable choices of the shape of the channel, descriptions of converging cylindrical and spherical shocks were obtained. These descriptions had good agreement with the similarity solutions valid near the points of collapse of shocks.

C. E. Smith [9] operated an experimental study of the starting process in a reflected-shock tunnel, and compared the results with numerical previous calculations. Results showed that an unsteady expansion wave dominated the transient flow and the shock wave played a minor role. It was found that initial pressures which were larger than the steady-flow static pressure could be tolerated without prolonging the starting process even though there was the presence of a strong secondary shock wave. F. Higashino [10] et al aimed at experimentally investigating both the development and the oscillation phenomena of pseudo shock waves in a two dimensional asymmetric nozzle. One case was both side walls of the diverging nozzle and the other was only one side wall diverging. It was found that an oblique shock wave appeared near the turning corner of the diverging section owing to a separation vortex and then it developed into a pseudo shock wave. The supersonic flow that issued from the duct was not much expanded in the flow direction and behaved like an under expanded jet which was deflected towards the shorter wall of the nozzle.

This paper mainly aimed at observing and analyzing shock wave propagation and validating effects of diaphragm pressure ratio on shock wave strength. Pressure measurement and schlieren visualisation were operated in the present experimental study. Pressure measurement was used to quantitatively analyse shock wave strength and shock wave propagation. Shock wave structure was qualitatively investigated by schlieren visualization. Different diaphragm pressure ratios were varied to be performed in present experimental model.

2. Experimental Method

2.1. The CST device

The needle-free drug delivery system is based on the Contoured Shock Tube (CST) as is shown in Fig 2. (a). In order to deliver drug particles into the skin with a narrow range of velocities, they must be accelerated and delivered in a quasi-one-dimensional steady flow field. The CST system consists of a micro shock tube and an expanded supersonic nozzle. Generally, two diaphragms must be needed in the micro shock tube and particles are seeded into the region between these two diaphragms. The diaphragm near the high pressure section is manually ruptured by using a needle. The second diaphragm is always naturally ruptured due to high pressure produced by the shock wave moving into the particle chamber. After two diaphragms are ruptured, particles together with the gas are accelerated behind the shock wave. High momentum of particles is obtained as they move through the supersonic nozzle so that they can be penetrated into the skin.

2.2. Pressure measurement

The experimental setup for pressure measurement is shown in Fig 2 (b). Six high sensitive pressure transducers were used to record the pressure change as shock waves move through the test section. The gauges were used to
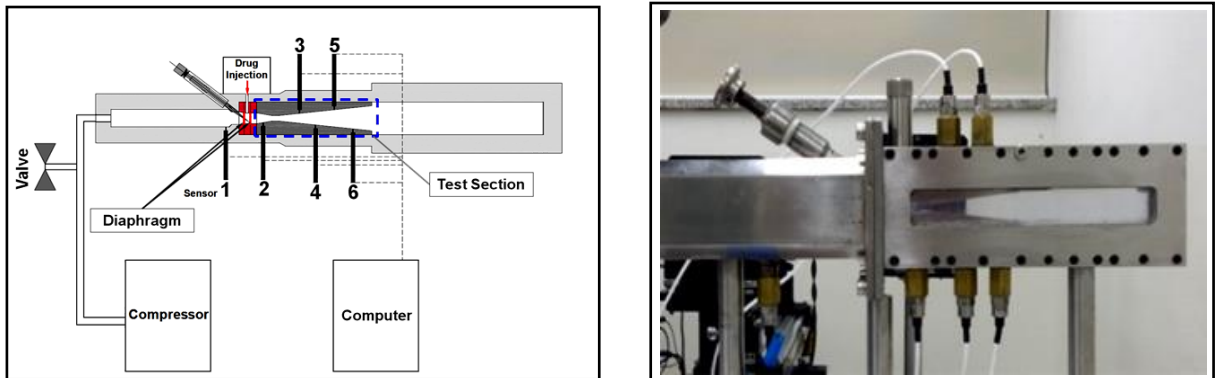
Fig. 2. (a) Schematic of pressure measurement; (b) Experimental setup for pressure measurement
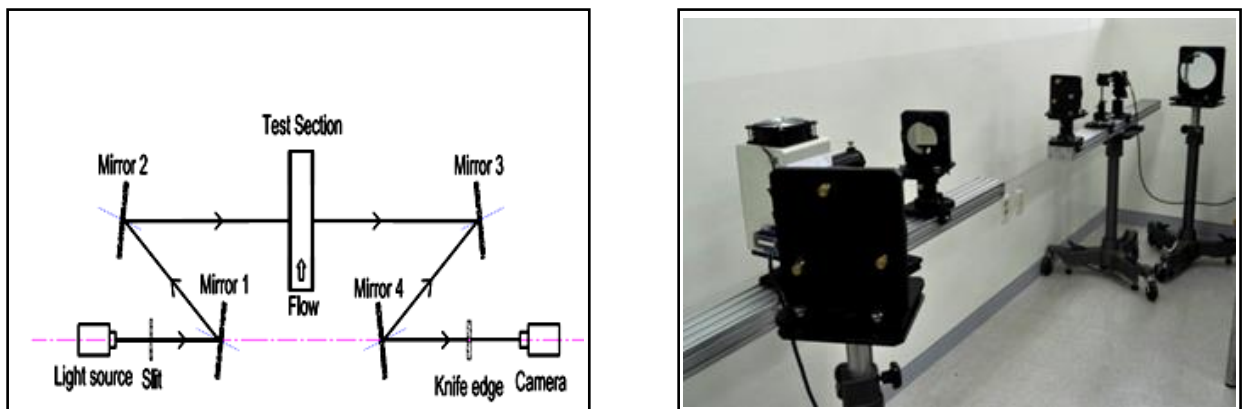

Fig. 3. **(a)** Schematic of Schlieren imaging system; (b) Experimental setup for Schlieren visualization

measure the static pressure at various locations in the device. Based on the distance between two transducers and time difference caused by that the shock wave moves through these two locations, the velocity of the shock wave can be easily obtained. Kulite pressure transducers (Kulite, XT-190) were mounted in the CST walls. Transducer 1 lied in the high pressure section with the pressure of P_4 and the other 5 were installed in the low pressure section with the atmosphere pressure of P_1. Transducer 2 located in the convergent section of the CST, and transducer 3, 4, 5, 6 lied in the divergent section of the CST.

2.3. Schlieren visualization

Schlieren imaging is a method to visualize density variations in transparent media. The optical setup of the present schlieren imaging system comprises five main sections including light source, mirrors, test section, knife edge and camera as is shown in Fig 3. (a) and (b). The parallel beam was achieved by a laser focusing into a pinhole and reflected by flat mirrors. A laser (OPS-500X-SP) delivering 20 ns pulse in synchro-nisation with the CCD camera was used as the light source for the experiment. A Nikon ED high speed Charge Coupled Device (CCD) camera was used to record up to 4000 schlieren images in each experiment at 20000 frames per second. To make schlieren imaging inside the expanded nozzle, the test section with a transparent square-section nozzle was constructed as is shown in Fig 2. (b). Glasses are used for transparent windows. The density change indicating shock wave structure is caught by schlieren imaging technique.

3. Results and Discussions

Pressure histories of six sensors at different diaphragm pressure ratios are shown in Fig. 4-6. Different initial high pressures were performed in the high pressure chamber from compressor. P4 was respectively initialized at the pressure of 21.5bar, 30.5bar and 40.3bar and P1 was kept a constant of atmosphere pressure for three experimental cases. After the first diaphragm was ruptured by the needle, the shock wave moved towards the region between two diaphragms, so that a high pressure was developed instead of the initial atmosphere pressure in this region. The second diaphragm was naturally ruptured. As the shock wave moved through the location where a pressure transducer was mounted, the pressure change was recorded.

The recorded pressure values of sensor 1 are clearly shown the initialized pressure in high pressure section. Pressure of sensor 1 kept a constant at the beginning, and gradually decreased later. This is mainly due to that expansion waves generated by the rupture of first diaphragm moved through the sensor 1. Pressure of sensor 2 increased after shock wave moved through this location. As the diaphragm pressure ratio increases, maximum pressure value of sensor 2 also increases. Pressure values of transducers change as the shock wave moves through these locations in the expanded supersonic nozzle. Based on time different between first steep peaks in pressure histories of two sensors and their distance, the shock wave velocity can be obtained. According to the time when the pressure started changing at the location of sensor 2, it is much less at the pressure ratio of 40.3 compared to that at the pressure ratio of 21.5 and 30.5. This indicates as the diaphragm pressure ratio increases, the velocity of shock wave also increases.

The trend of pressure change for sensor 3, 4, 5, 6 is almost similar. As the shock wave moved through these locations, the pressure increased. After reaching the peak value, it decreased. This results from that the supersonic flow behind the shock wave was accelerated as it went through the divergent section of the expanded nozzle. Flow is initiated by the primary shock wave, which opens a transient starting process of the type described by Smith (1966) and Amman and Reichenbach (1973). This phase is followed by a quasi-steady supersonic flow during which static pressure decreases as total pressure decays [1]. The pressure increased again due to the high pressure gas moved through the divergent section. Finally it kept a constant after all waves moved outside from the test section.

Sequences of schlieren images are shown in Fig. 7. Shock wave propagation can be clearly seen from these images. The flow moved from the left to the right. The flow density gradient distributions show the structure of shock waves. In the Fig. 7 (a), a clear primary shock wave produced by the rupture of the second diaphragm propagated in the divergent section of CST at t=0.8334. In the Fig 7 (b), 1.6057 ms later, due to the supersonic flow moved through the divergent section, weak oblique shock wave was observed. The oblique weak shock happened reflection along the nozzle walls, which can be obviously observed. This shock system forms the subsequent quasi-steady supersonic flow after the primary shock left the divergent nozzle.

As the supersonic flow moved through the exit of the expanded supersonic nozzle, relatively strong oblique shock occurred. A normal shock developed in the front of the strong oblique. This is results from that supersonic flow occurred in the front of the strong oblique shock. Based on shock wave theory, the supersonic flow can be obtained behind the static oblique shock as supersonic flow goes across this oblique shock at the weak solution. The oblique shock happened reflection, which can be easily seen from Fig 7. (c). In addition, the reflected shock waves became weak. This mainly results from the viscous effects of the flow and the friction between the front edge of oblique shock waves and the walls. The decay of shock wave strength leads to a small density gradient change of the flow, so that weak shock waves are not obviously shown in images. Oblique shock system consisted of at least four oblique shock cells in Fig 7. (d). Similar starting process shock structures have been observed and investigated by Gvozdeva and Zhilin (1977) and Britan and Vasilev (1986). This oblique shock system dominating the starting process exists as a result of the expanded nozzle operation [1].

A derived normal shock occurred as is shown in Fig. 7 (e). This is mainly due to that the shock tube is open at the end of shock tube exit. Pressure gradually decreased from the shock tube exit to the high pressure chamber. The
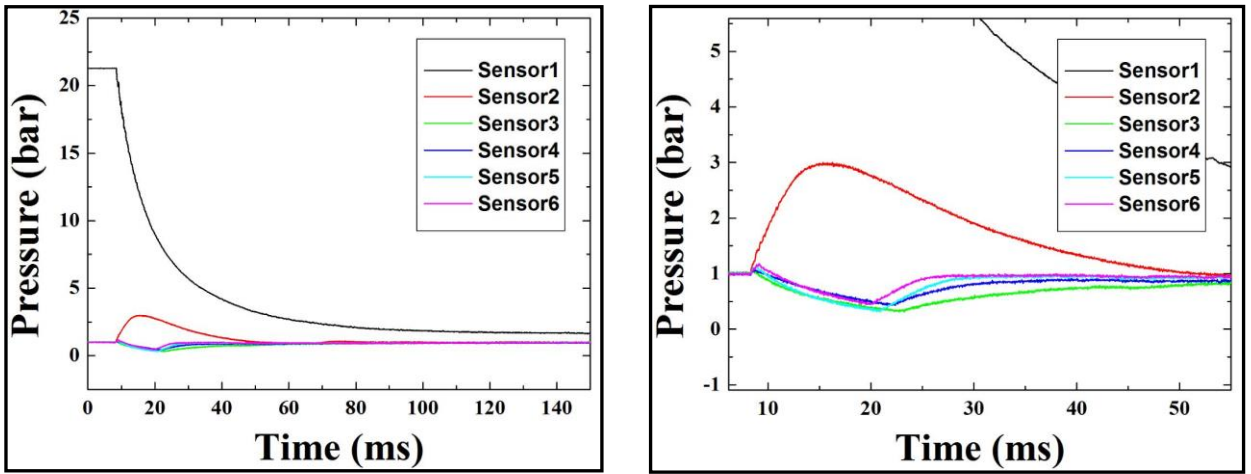
Fig. 4. Pressure histories of pressure sensors at diaphragm pressure ratio of 21.5 (P_1=1 bar)
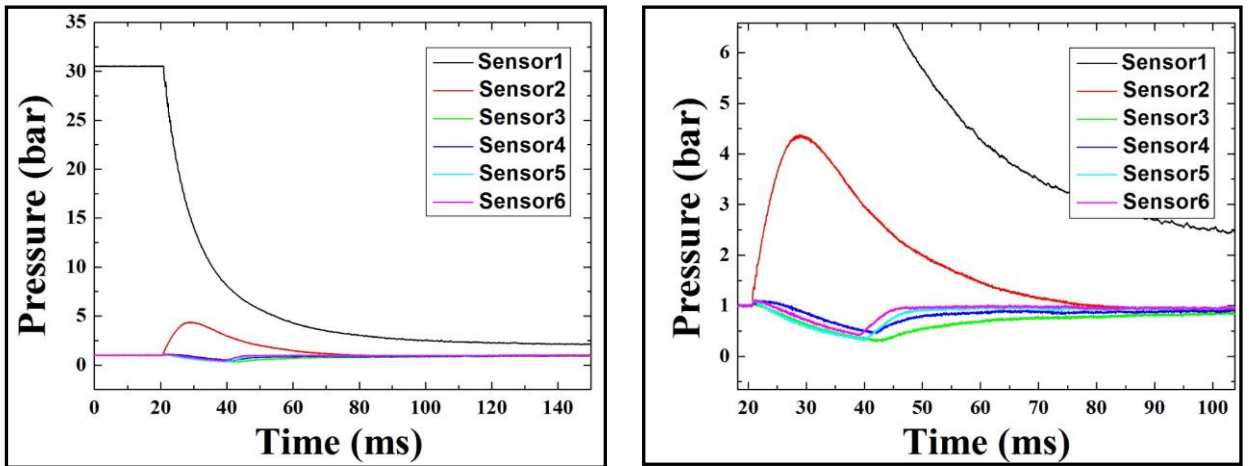

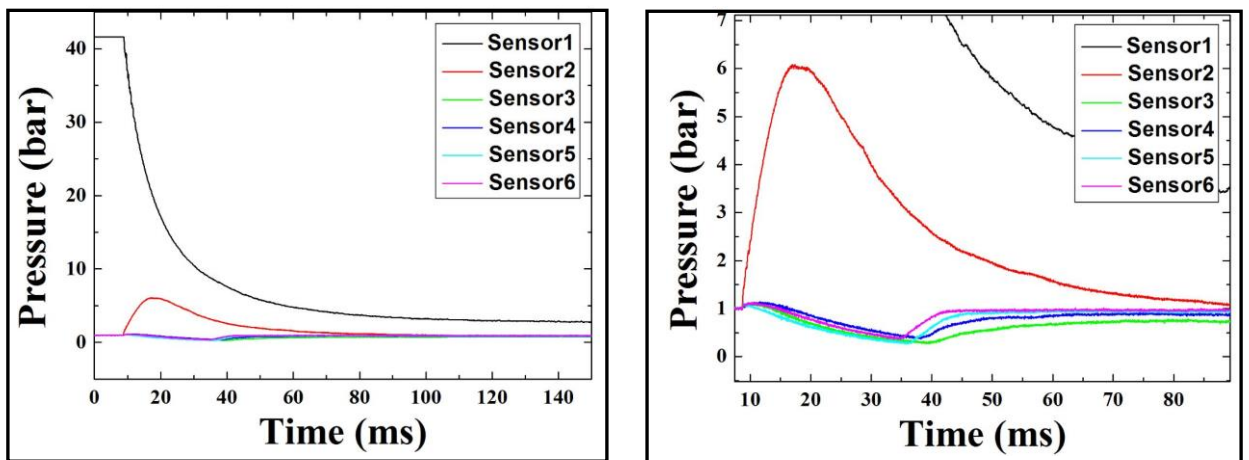Fig. 5. Pressure histories of pressure sensors at diaphragm pressure ratio of 30.5 (P_1=1 bar)

Fig. 6. Pressure histories of pressure sensors at diaphragm pressure ratio of 40.3 (P_1=1 bar)

(a) t = 0.8334ms

(b) t = 1.6057ms

(c) t = 1.8613ms
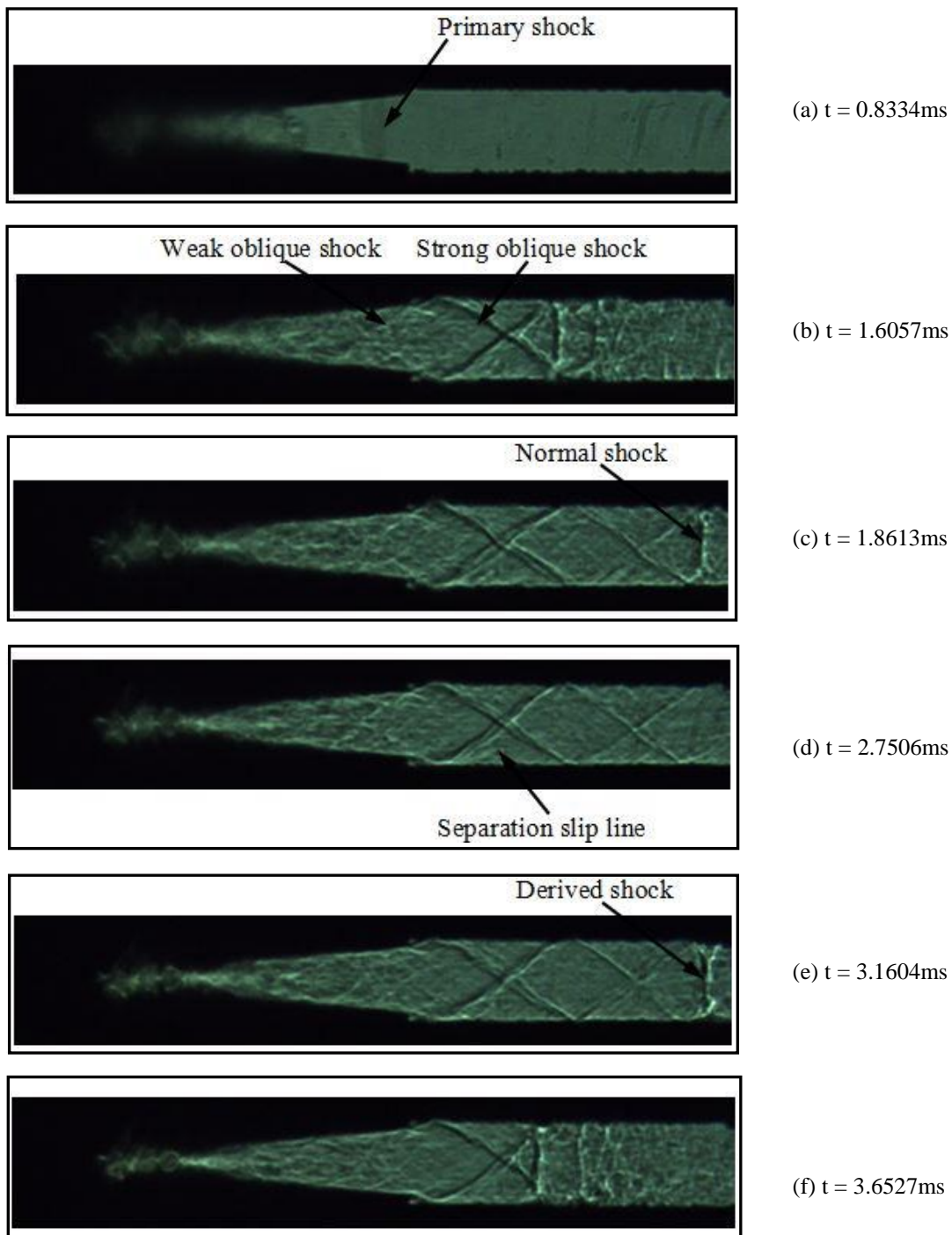
(d) t = 2.7506ms

(e) t = 3.1604ms

(f) t = 3.6527ms

Fig. 7. Schlieren images at variable time at diaphragm pressure ratio of 21.5

derived normal shock moved towards the opposite direction compared to the primary shock. The derived shock propagation is easily observed in Fig. 7 (e) and (f). Based on the time difference and the distance of shock wave moving in these two images, the velocity of derived shock can be obtained.

4. Conclusions

Pressure measurement and schlieren visualization have been used to investigate the flow dynamics inside a Contoured Shock Tube. Pressure histories were obtained at different locations in the CST at different diaphragm pressure ratios. Results showed that as the diaphragm pressure ratio increases, the shock velocity also increases. This has a good agreement with the shock wave theory. The region showing a quasi-steady supersonic flow where the static pressure decreased was observed in the pressure measurement. Schlieren images revealing the structure of oblique shock waves and reflected shock waves were obtained in present experimental study. The density gradient distributions were clearly shown in schlieren images. The primary normal shock was clearly observed. The oblique shock system dominating the starting process existed as a result of the expanded nozzle operation was also obtained. As the oblique shock wave happen reflection, the shock strength gradually decreases. This is mainly due to viscous effects of the flow and the friction between the front edge of oblique shock waves and shock walls. More experimental tests will be performed to understand shock wave propagation and flow characteristics in the present experimental model. Numerical simulation will be also made to compare with experimental results.

5. Experimental Uncertainty

The pressure measurement and schlieren visualization technique were used to observing shock wave propagation and internal flow in the needle-free delivery system. Because of manual rupture of diaphragms used in present experiments, the vibration of measured device happened in the experimental system. This could affect recorded data from pressure transducers and quality of images for camera. In addition, the response time of pressure transducers also had great effect on pressure measurement and accurate results will be obtained from high-sensitive pressure transducers. Resolution of the camera is a very important parameter for high-quality images. As shock wave moved, density changed in the front and after shock wave, which was taken by the camera. High resolution one could apply detailed change in images. The trigger used for combining the laser and the camera is an anther important part and suitable coupling between the laser and the camera must be needed. Those effects led to uncertainty in present experimental results. For the future experimental tests, those effects should be considered and improved so that good results will be obtained.

Acknowledgments

References

[1] M. A. F. Kendall, N. J. Quinlan, R. W. Thorpe, S. J. Anisworth, and B. J. Bellhouse, Measurements of the gas and particle flow within a converging-diverging nozzle for high speed powdered vaccine and drug delivery, Experiments in Fluids, vol. 37 (2004) 128-136.

[2] M. A. F. Kendall, The delivery of particulate vaccines and drugs to human skin with a practical hand-held shock tube-based system, Shock Wave, vol.12 (2002) 23-30.

[3] Y. Liu, Performance studies of particle acceleration for transdermal drug delivery, Med Bio Comput, vol.44 (2006) 551-559.

[4] Y. Liu, and M. A. F. Kendall, Numerical analysis of gas and micro-particle interactions in a hand-held shock-tube device, Biomed Micro devices, vol. 8 (2006) 341–351.

[5] Y. Liu, M. A. F. Kendall, N. K. Truong and B. J. Bellhouse, Numerical and experimental analysis of a high speed needle-free powdered vaccines delivery device, 20th AIAA Applied Aerodynamics Conference, St. Louis, Missouri, 24-26 June, 2002.

[6] M. C. Marrion, M. A. F. Kendall and Y. Liu, The gas-dynamic effects of a hemisphere-cylinder obstacle in a shock tube driver, Experimental in Fluids, VOL. 38 (2008) 319-327.

[7] N. J. Quinlan, M. A. F. Kendall, B. J. Bellhouse and R. W. Anisworth, Investigation of gas and particle dynamics in first generation needle-free drug delivery device, Shock Wave, vol.10 (2001) 395-404.

[8] R. F. Chisnell, The motion of a shock wave in a channel with applications to cylindrical and spherical shock waves, Journal Fluid Mechanics, vol. 2 (1957) 286–298.

[9] C. E. Smith, The starting process in a hypersonic nozzle, J. Fluid Mech, 24(4) (1966) 625-641.

[10] F. Higashino, S. Matsuo and T. Tsuyuki, Oscillation of oblique shock waves generated in a two dimensional asymmetric nozzle, SAE Transactions, vol. 100 (1991) 2254–2262.

6th BSME International Conference on Thermal Engineering (ICTE 2014)

Numerical Study of Sub-Nozzle Flows for the Weft Transmission in an Air Jet Loom

Jin Hyeon Kim[a], Toshiaki Setoguchi[b] and Heuy Dong Kim[a*]

[a]*Department of Mechanical Engineering, Andong National University, Andong 760-749, Korea*
kimjh1@anuis.andong.ac.kr[1], kimhd@andong.ac.kr[1*]
[b]*Department of Mechanical Engineering, Saga University, Saga, Japan*
setoguci@me.saga-u.ac.jp
Corresponding author: Prof. Kim, Heuy Dong (kimhd@andong.ac.kr)

Abstract

The air jet loom is widely applied in the textile industry due to its high productivity, convenient controllability, high filling insertion rate, low noise and low vibration levels. High-Speed air jet weaves the weft yarn, and transports it through the weft passage. In the present study, a computational fluid dynamics method is applied to solve the incompressible Navier–Stokes equations with one-equation Spalart-Allmaras turbulence model. Which is used to solve the flow filed in a weft passage. The aim of this analysis is to determine the distribution of the flow velocity along the weft passage. Results revealed the strong relationship between air jet velocity and forces on the weft.).

Keywords: Air Jet Weft Insertion, Main Nozzle, Sub Nozzle, Air Jet Loom, Profile Reed

Nomenclature

dF_f	fiction force [N]
c_f	drag coefficient for the surface [-]
τ	shearing stress [N·m^{-2}]
D	nozzle diameter [mm]
ρ	density [k·g·m^{-3}]
u	air jet velocity [m·s^{-1}]

v	weft velocity [m·s^{-1}]
X	weft length [mm]

1. Introduction

According to the set intermittent operation of the air jet loom weaving machine, the structure is designed based on the characteristics of the weft insertion of the weaving machine. Air-jet weft insertion systems are currently used in all kinds of fibres and yarns. The weft is moved by the friction created by the high speed flow of the air jet loom. The air jet force is required to move and accelerate the weft yarn.

These forces should be higher than the inertia and resistance. It is defined in consideration with the characteristics and physical properties of the air flow, and resistance properties. The actual air speed depends on the properties such as turbulent air flow or laminar flow, a constant thread diameter, linear density and elasticity. The complex relationship between the air flow speed and productivity of weft in important [1,2]. It is controlled so as to change the count and twist factor at all times. If the twist coefficient increases, and the speed of the weft is reduced the average speed is a goes up [3].

The first commercial system introduced by Max Paabo Maxbo air jet loom that is 80cm in width cloth surface to 350Hz display in Sweden in 1951. It was charged with developing the main nozzle insert, shaped cross-sectional profile of the sub nozzles and U- lead system by a German company in 1969 in Te Strake. The role of the flow guide channel with recessed groove portion of the lead body in profile was also modified. When using a profile reed it is not necessary for separation of the guide rings, and to solve the problem in which it passes through a ring of air flow guide system slope method.

The combination of low manufacturing requirements and high performance of air-jet loom has many advantages, such as inserting a very high speed, high productivity and low initial expenditure, a simple operation of moving parts, reduced risk, low noise and vibration levels. The changes depending on the development status of air-jet looms, which focuses on the interaction between the guidance system to increase of the speed of the yarn is mainly on air speed.

Driving force with the velocity of the air jet was obtained by performing a numerical analysis for the sub nozzles in this study. Improving speed due to the change in the radius of the air-jet nozzle and the width of the next sub and drive were focused on.

2. Theoretical Analysis

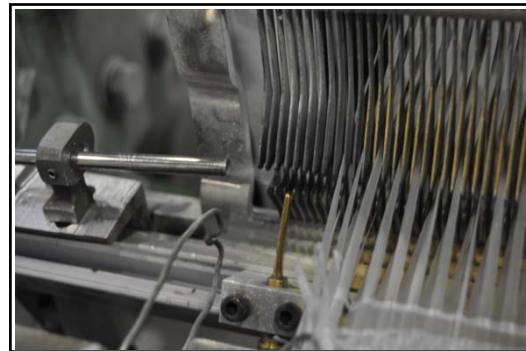Fig. 1. The setup of air jet loom equipment.

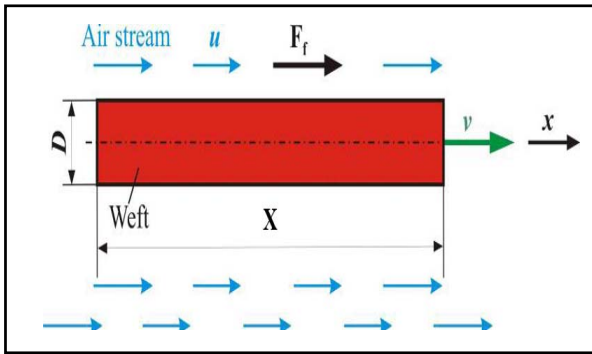Fig. 2 Positions of the main nozzle and the sub nozzle.

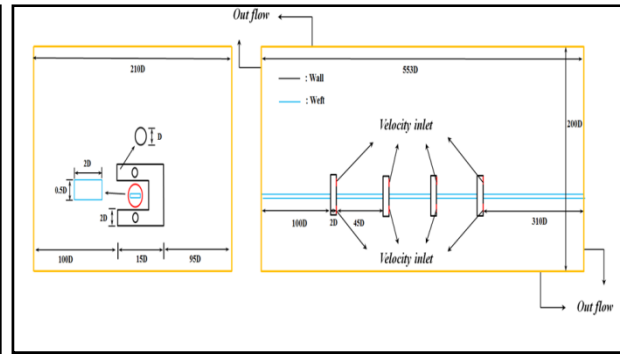Fig. 3 Schematics of the jet force on a moving weft.   Fig. 4 Computational domain and boundary conditions of the sub nozzle.

The kinetic energy of the compressed air is generated by the nozzle. To obtain the high speed, the weft is ejected from the nozzle at the center of the circular cross section air holes. A viscous shearing boundary layer is created between the surfaces due to the friction force of the flowing medium. It is determined based on the friction force of the surface where the weft is generally applicable [4] .

$$dF_f = c_f \cdot \tau \cdot dA \tag{1}$$

At the same time, the diameter D of the weft is defined based on the weft length dx.

$$dA = D \cdot \pi \cdot dx \tag{2}$$

Based on Bernoulli's equation, shear stress is generated in the weft and the air jet is moved.

$$\tau = \frac{1}{2} \cdot \rho \cdot (u - v)^2 \tag{3}$$

However, since the weft speed is ignored in this study, the shear stress is also ignored. because our studies were made for motionless weft [5].

$$\tau = \frac{1}{2} \cdot \rho \cdot u^2 \tag{4}$$

The driving force for weft yarn moving in air jet is shown in Fig.3 by the friction between the air and the chamber surfaces.

$$F_{fr} = \frac{\pi}{2} \cdot \rho \cdot c_f \cdot D \cdot X \cdot u^2 \tag{5}$$

The space between the air stream and the thread is proportional to the square of the relative velocity and the Reynolds number and varies depending on the surface friction coefficient of the driving force. Because deviation from the center of the flow chamber slows down the moving speed of the weft, the turbulence of the air flow will be reduced. Therefore, the turbulent flow is very small. But it is impossible because of the air speed of the inserting

yarn is very low, [3].

3. Numerical methods

In this study, the visualization of the secondary nozzle flow was performed in a three-dimensional domain. Incompressible, NS equation were used to compute the flow in the sub nozzles of air-jet looms. Numerical calculations using commercial software Fluent Ver. 15 was used, with Coupled Implicit method, in order to compensate for the numerical instability. The present numerical analysis has already been applied in the literature AUSM-DV and 2nd Order Up-Wind Scheme is applied. Outflow, boundary conditions were applied at the exit of the domain, Velocity inlet is applied for the nozzle inlet with No-slip and adiabatic were condition. The details are shown in the Table 1, in terms of the sub nozzle variables and conditions. Inlet total pressure (P_{t1}) of 5bar, 7bar, 9bar, 11bar, diameter of nozzle (d) 1mm, 1.5mm, 2mm are used and the outlet pressure kept at 1bar.

Table 1. Structural variables of the sub nozzle.

Diameter of nozzle(mm)	angle(degree)	P_{t1}(bar)	P_{t2}(bar)
1, 1.5, 2	12.1, 14, 16.69	5,7,9,11	1

4. Results and discussion

4.1 Sub Nozzle

Numerical analysis was performed to investigate the velocity distribution and the driving force of the sub nozzles. The inlet pressure of the nozzle (P_{t1}) is 7bar, the nozzle outlet pressure was set at atmospheric pressure (P_{t2}) is. The results of velocity of the air stream in the weft passage are provided as following.
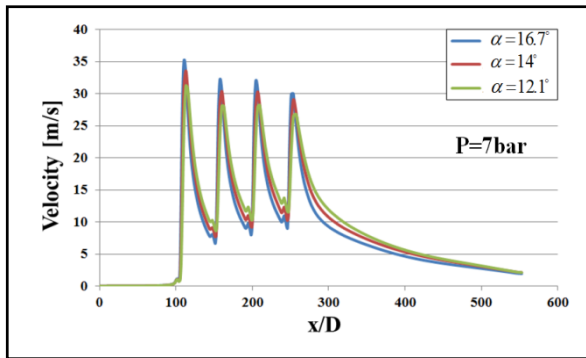

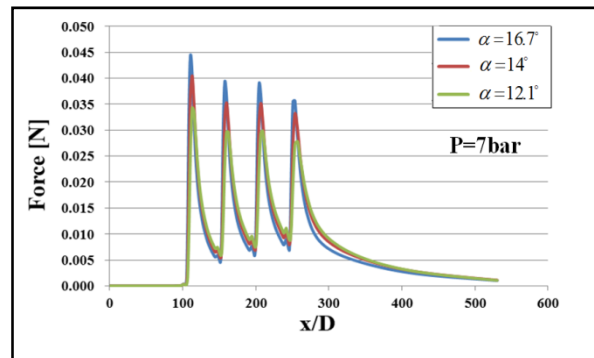Fig. 5 Velocity distribution along the weft wall of 3D sub-nozzle.

Fig 6. Force distribution along the weft wall of 3D sub-nozzle.
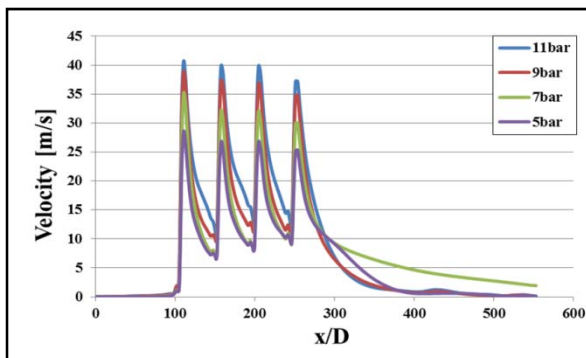

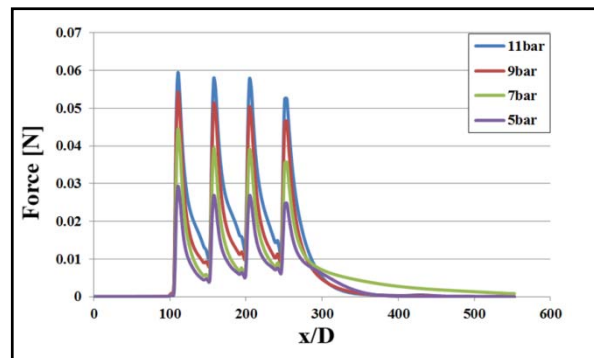Fig. 7 Velocity distribution along the weft wall of 3D sub-nozzle.

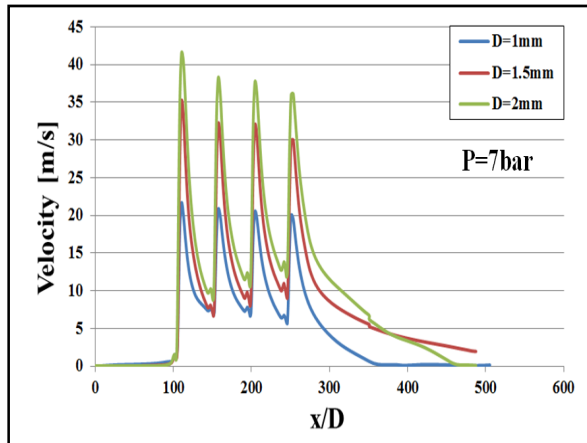Fig. 8 Force distribution along the weft wall of 3D sub-nozzle.

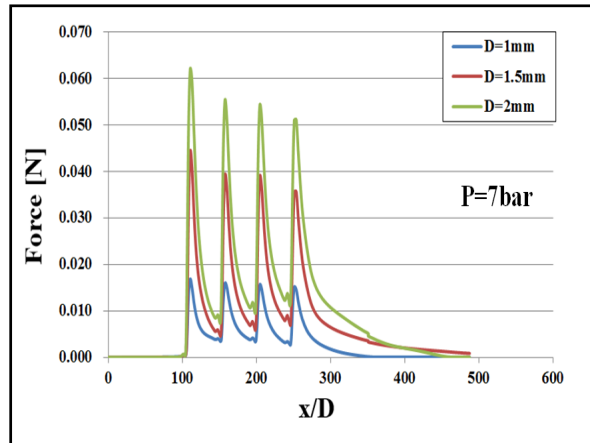Fig. 9 Velocity distribution along the weft wall of 3D sub-nozzle.

Fig 10 Force distribution along the weft wall of 3D sub-nozzle.

4.2 Velocity distribution vs. angle of the air jet

The velocity distribution along the weft passage is plotted in the Fig. 5 with change in air jet angle. The plot shows an increase in speed abruptly in the vicinity of the auxiliary nozzle. The larger the angle of the air jet, the larger in the magnitude of the velocity. The velocity before the sub nozzle is zero because of the absence of the main nozzle i n the present CFD study. Fig. 6 represent the calculated results from Eqn. 5. The velocity of the air jet has a great inf luence on the driving force of the sub nozzles, which is observed from the results. The force is increased due to the e xistence of the sub nozzles and sharp increment can be found near the exit of the sub nozzles.

4.3 Velocity distribution vs. pressure change

Jet flow velocity distribution of the air in the weft passage with inlet total pressure change is shown in Fig.7. Increas e in pressure resulted in higher speed. The maximum rate per minute highest at 11bar and is approximately 2400m/ min. It was found to be about twice the velocity of the field. Fig.8 shows the change of the driving force due to press ure. The velocity distribution in the weft passage showed a similar trend, and as the pressure was increased the drivi ng force was also greater.

4.4 Velocity distribution vs. change in nozzle diameter

Air jet flow speed distribution in the weft passage with change in the nozzle diameter is shown in Fig. 9. Increases i n of the auxiliary nozzle dramatically increase the velocity. The results shown by equation (5) it reveals the driving f orce with changing diameter in Fig.10 and shows a tendency similar to the velocity distribution under the influence of the air jet. It is found that higher driving forces are also generated at higher diameter.

5. Conclusions

 In this study, a numerical analysis has been performed by changing the pressure, nozzle diameter and jet angle of the sub nozzle in order to visualize the flow in an air jet loom. Present results are summarized as follows:

1) A large impact of the air jet velocity on the force for weft transfer in observed.
2) Larger air-jet nozzle angle increases the air jet velocity and the driving force at the surface of the weft.
3) As the sub nozzle pressure increase, the jet speed on the weft surface also increases.
4) As the diameter of the sub nozzle exit increases the air jet velocity comes out at higher momentum.

References

[1]   Adanur, S. and Mohamed, M. H., "Analysis of Yarn Motion in Single-nozzle Air-Jet Filling Insertion", Part II: Experimental Validation of the Theoretical Models and Statistical Analysis, Journal of the Textile Institute, Vol. 83, No. 1 (1992) pp. 56-68.
[2]   Adanur, S. Handbook of Weaving. Sulzer (2001) 177-201
[3]   Adanur, S., and Mohamed, M. H., "Weft Insertion on Air-jet Looms: Velocity Measurement and Influence of Yarn Structure", Part II Effects of System Parameters and Yarn Structure, Journal Textile Institute, No 2 (2001) pp.73-93.
[4]   Y. Liu, and M. A. F. Kendall, Numerical analysis of gas and micro-particle interactions in a hand-held shock-tube device, Biomed Micro devices, vol. 8 (2006) 341–351.
[5]   Lorant, S., Istvan, P., and Ggbriella, O., "The Dynamic Study of the Weft Insertion of Air Jet Weaving Machines.", Acta Polytechnica Hungarica, Vol. 7, No. 3 (2010) pp. 93-107
[6]   Lorant, S., Laszlo, S., "Weft Insertion Through Open Profile Reed in Air Jet Looms.", Electronic Journal of Environmental Sciences, 6 (2012)
[7]   Colak, O., Kodaloglu, M., "Velocity Control of Weft Insertion on Air Jet Looms by Fuzzy Logic.", University of Suleyman Demirel Department of Textile Engineering, Vol. 12, No. 3 (2004) pp. 29-33.

6th BSME International Conference on Thermal Engineering (ICTE 2014)

An Empirical Model for Annular Flow in Gas Wells

Aziz Rahman*

Assistant Professor, Memorial University of Newfoundland, 240 Prince Philp Dr., St John's, NL, A1B 3X5, Canada

Abstract

In annular flow of a natural gas well, liquid may be present in entrained droplets as well as in the film near to the well wall. A number of models have been proposed over the past 50 years to predict film thickness in pipes with vertical two-phase annular flow. Earlier models are based on correlations from the limited range of experimental data. The proposed modified film thickness model developed from a range of experimental data. The experimental data covers conditions of superficial liquid velocities ranging from 0.6×10^{-3} to 0.39 m/s; superficial gas velocities ranging from 13.4 to 110.6 m/s; and diameters ranging from 12 to 51 mm. The proposed model is compared with the available experimental data in the literature. Model predictions are in good agreement with the available experimental data set. The modified film thickness model helps to explain the fundamentals of annular flow, which in turn is beneficial to the natural gas production industry as it further develops the understanding of production mechanics.

1. Introduction

Past attempts to quantify liquid base film thickness (δ) in a two-phase system have been greatly improved upon resulting in significant progress in modelling natural gas transportation behaviour. There are numerous models to determine film thickness. Schubring et al. [1] completed a series of experiments using optical techniques, which measured base film thickness in annular two-phase flow.

* Corresponding author. Tel.: +1-709-749-7497; fax: +1-709-864-8975.
  E-mail address: marahman@mun.ca

Nomenclature

A	Area (m^2)
D	Diameter (m)
E	Entrainment rate (-)
Fr	Froude Number (-)
g.	Gravitational acceleration (m/s^2)
m	Mass flow rate (kg/s)
Re	Reynolds number (-)
U	Velocity (m/s)
We	Weber number (-)
x	Flow quality (-)
y	Radial coordinate (m)
δ	Film thickness (m)
ϵ	Roughness (m)
μ	Viscosity (kg/m.s)
v	Kinematic viscosity (m^2/s)
ρ	Density (kg/m^3)
σ	Surface tension (N/m)
τ	Shear stress (Pa)

In these experiments horizontal and vertical conditions were examined and a correlation for each case was determined. The experiments included measuring superficial gas velocity against film thickness at fixed superficial liquid velocity values. This type of experiment included 3 horizontal cases using inside tube diameters of 8.8mm, 15.1mm, and 26.3mm and a vertical case having an inside diameter of 23.4mm. Schubring *et al.* [1] developed a model using an empirical correlation to calculate the film thickness. However, dependency on the critical friction factor in calculating the film thickness incorporates an iterative process and an initial film thickness estimate is required to find the final film thickness. This can be seen in the following set of equations.

$$\frac{\delta}{D} = 4.7 \frac{1}{x} \left(\frac{\rho_g}{\rho_l} \right)^{1/3} \text{Re}_G^{2/3} \tag{1}$$

$$\text{Re}_G = \frac{GD}{\mu_l} \tag{2}$$

$$x = \frac{m_g}{m_g + m_l} \tag{3}$$

$$G = \frac{m_g + m_l}{A} \tag{4}$$

From the above equation it is observed that an initial film thickness must be estimated in order to calculate the Reynolds number. Based on the findings, Schubring *et al.* [1] concluded that base film thickness is most strongly connected to gas flow and the effect of liquid flow rate is significant at lower gas flows. Typical base film thickness uncertainties for the horizontal tube were around 2% for high gas flows. Uncertainties were higher in the vertical tube (approximately 15%) due to the decreased wall thickness.

Expanding upon their past research, Schubring *et al.* [2] conducted another series of experiments using planar

laser-induced fluorescence (PLIF) in a vertical tube with an annular flow regime of an air-water mixture in order to quantify the liquid film thickness. By introducing fluorescent dye into the water, the thin film layer could be measured after a series of images were processed. By detecting the presence of the dye at the surface of the film the thickness could then be determined. This experimental method proved advantageous over past methods as it allowed for a visual of the film after processing, which showed the differences between the base film and the waves that are observed during annular flow. The data obtained was applied to the Wallis [3] single-zone interfacial shear correlation, the Owen and Hewitt [4] correlation, and finally, the two-zone model by Hurlburt *et al.* [5]. For the Wallis [3] correlation, results at low liquid flow rates are consistent with experimental data. However, for high liquid flow rates the Wallis [3] model is not suitable for annular flow film thickness predictions due to its inconsistencies with the experimental data. Typically the Owen and Hewitt [4] correlation, essentially a more complex version of the Wallis correlation, uses the entrainment fraction as an input to output film height and pressure loss, however, by using film height as an input, the entrainment fraction and pressure loss are found. It was observed that the Owen and Hewitt [4] correlation performed similarly to the Wallis [3] correlation in that for low liquid flow rates the predictions for pressure loss are consistent with experimental data; however, at high liquid flow rates the model diverges. The analysis noted that the Owen and Hewitt [4] model was no better than other correlations.

From the analysis, Schubring *et al.* [1] concluded that average film thickness was found to be an increasing function of liquid flow rate and a decreasing function of gas flow rate. This paper proposes a new film thickness model that has been developed by correlating to a wide range of experimental data. This model is based on Reynolds, Weber, and Froude dimensionless numbers and requires only diameter, fluid properties, and flow rates as inputs.

2. New model for film thickness

Based on existing experimental data, a new film thickness model was developed. This data comes from the works of Schubring *et al.* [1], [6]-[8], Bai & Newell [9], Alamu & Azzopardi [10], Paz & Shoham [11], and Butterwoth [12]. The experimental data covers conditions of superficial liquid velocities ranging from 0.6 to 38.8 cm/s; superficial gas velocities ranging from 13.4 to 110.6 m/s; and diameters ranging from 12 to 51 mm. The new film thickness model is based on Reynolds, Weber, and Froude dimensionless numbers and thus requires only diameter, fluid properties, and flow rates as inputs.

$$\partial_{mod} = 1.93 \times 10^{-3} (\text{Re})^{-0.246} (We)^{-0.161} (\dot{m}_L / \dot{m}_G)^{0.546} (Fr)^{0.15} \tag{5}$$

Where, $Re = \rho_g U_{sg} D / \mu_l$, $We = \rho_g U_{sg}^2 D / \sigma$, $Fr = U_{sl}^2 / gD$.

Previously proposed models rely on correlated methods and empirical data from experiments that cover a narrow range of data to determine base film thickness as well as wave thickness. The new film thickness model has been developed from past experimental results, which collectively cover a broad range of diameters, fluid properties, and flow rates. The new model therefore provides a better model than those previously proposed.

3. Results and Discussions

Results from the new model were compared with results presented by Schubring *et al.* [1], [6]-[8], Alamu and Azzopardi [10], and Butterwoth [12]. Each author has developed their respective film thickness models based on a series of experiments that use diameters that range from 19mm to 31.75mm. As such it is not acceptable to directly compare the values for experimental film thickness with the values calculated by the new model. In order to circumvent the inability to directly compare these values both experimental film thickness and modelled film thickness have been normalized with their respective diameters, and presented in the form of δ/D. The figure below represents a comparison between normalized values of experimental film thickness values and film thickness values calculated by the new model.
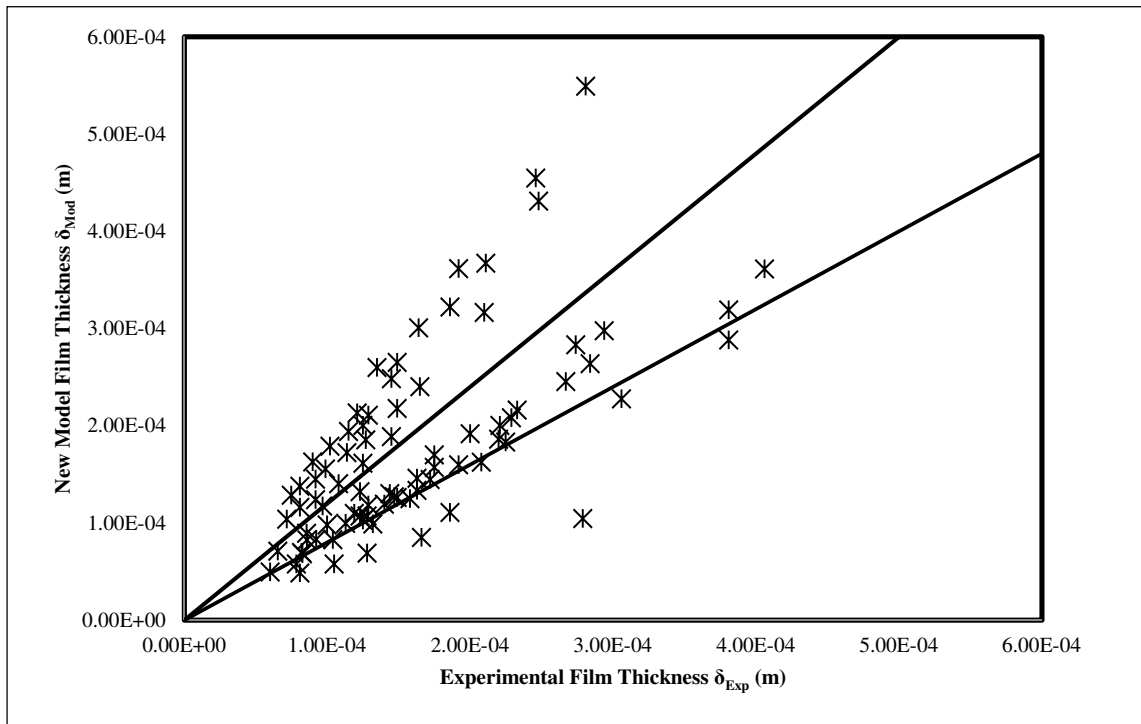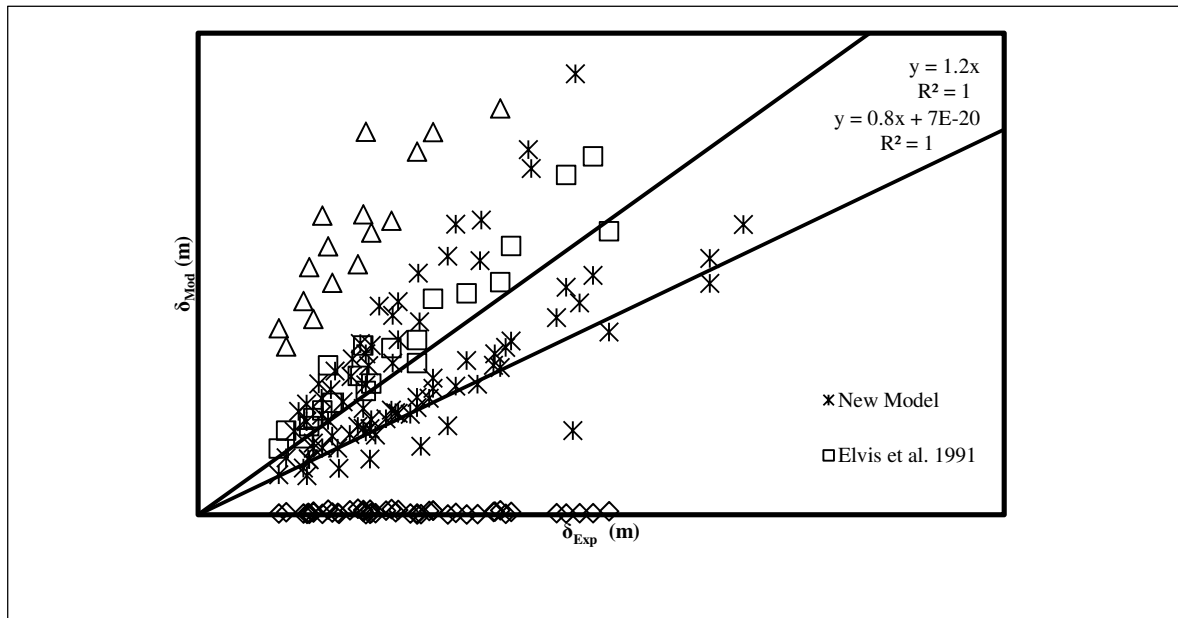
Fig. 1: Comparison of new film thickness model with experimental data

For complete agreement between experimental data and model results, the values from Fig. 1 would lay on the line y=x, however, it can be seen that the majority of the points in this figure lie within the +/- 20% tolerances. Therefore, the comparison between the new film thickness model and the experimental film thickness data reveals that the model is indeed an appropriate approximation of experimental film thickness values.
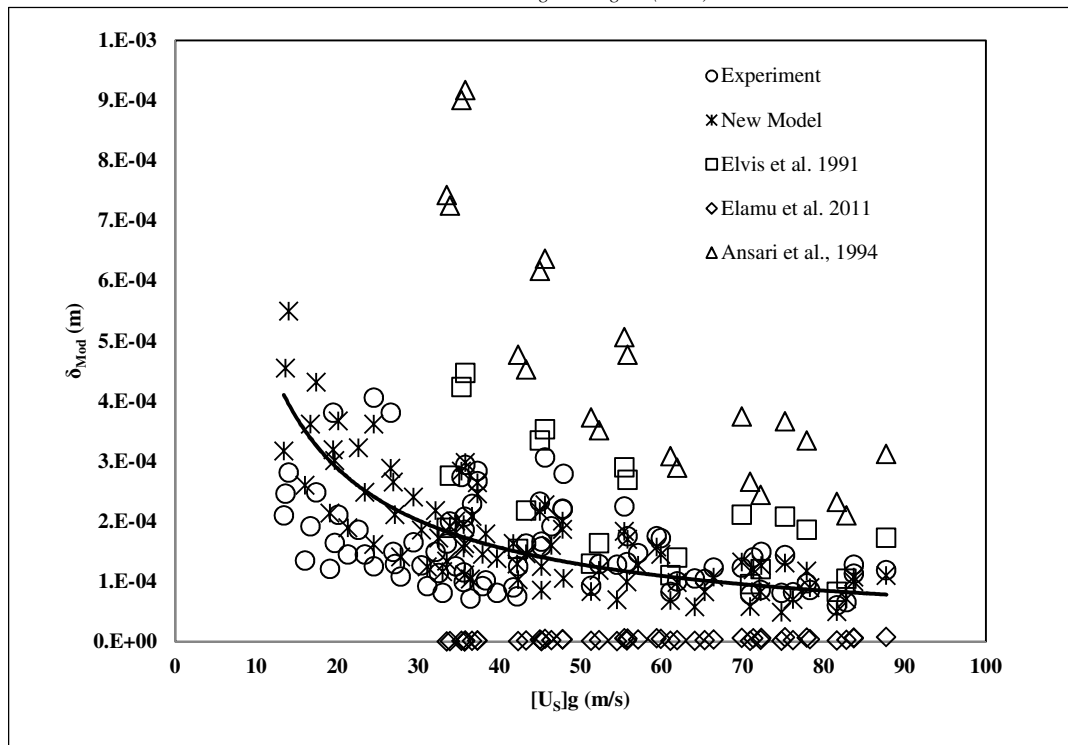
Fig. 3: Comparison of film thickness models with superficial gas velocity

Further analysis of the new model and past models developed such as Elamu *et al.* [10] and Ansari *et al.* [13], with experimental measurements of film thickness reveal that the new model does indeed provide better predictions compared to the existing models. Fig. 2 shows the comparison of film thickness models with experimental data and other models.

The comparison of film thickness models with experimental data and other models clearly shows that while the values for the new model mostly reside within the acceptable area of +/- 20% of experimental data, values from Elamu *et al.* [10] and Ansari *et al.* [13], reside outside this area. It can be noted that the models presented by Ansari *et al.* [13] show a tendency to over predict film thickness, while the model presented by Elamu *et al.* [10] greatly under predicts experimental film thickness values. The inability to predict experimental results from the models presented by Elamu *et al.* [10], and Ansari *et al.* [13] can also be observed in Fig. 3 by the interaction between film thickness and varying superficial gas velocity.

Due to the fact that the past models were developed for a smaller, narrower range of flow rates, the models' ability to predict experimental results deteriorates at higher flow rates with the exception of the model from Ansari *et al.* [13], which seems to converge towards experimental prediction with increasing superficial gas flow. The new model remains the more accurate model, as it does not appear to deviate from the film thickness trends captured by the experimental data therefore validating the use of this new model.

4. Conclusions

The conclusions from this study are as follows:
- A new model was developed to calculate the film thickness for annular flow.
- Hydrodynamic force balance was applied to develop the new model.
- The newly developed model can reliably predict experimental data compared to other models.
- The new model will help tremendously in the reliable prediction of gas well pressure gradient for a wide

range of operating conditions.

Acknowledgements

References

[1] D. Schubring, A. Ashwood, E. Hurlburt, T. Shedd, Optical measurement of base film thickness in annular two-phase flow, ASME Fluids Engineering Conference, Jacksonvill, Florida, 2008.
[2] D. Schubring, T. Shedd, A model for pressure loss, film thickness, and entrained fraction for gas-liquid annular flow, International Journal of Heat and Fluid Flow. 32: 3 (2011) 730-739.
[3] G. Wallis, One-dimensional Two-Phase Flow, New York: McGraw-Hill, 1969.
[4] D. Owen, G. Hewitt, T. Bott, Equilibrium annular flows at high mass fluxes; data and interpretation, PCH Physiochem. Hydrodynamics. (1985) 115-232.
[5] E.T. Hurlburt, L.B. Fore, R.C. Bauer, A two zone interfacial shear stress and liquid film velocity model for vertical annular two-phase flow, ASME 2006 2nd Joint U.S.-European Fluids Engineering Summer Meeting Collocated With the 14th International Conference on Nuclear Engineering, vol. 2, Miami, Florida, USA, July 17–20, 2006.
[6] D. Schubring, A. Ashwood, T. Shedd, E. Hurlburt, Planar laser-induced fluorescence (PLIF) measurements of liquid film thickness in annular flow. Part I: Methods and Data, International Journal of Multiphase flow. 36:10 (2010) 815-824.
[7] D. Schubring, T. Shedd, A. Ashwood, E. Hurlburt, Planar laser-induced fluorescence (PLIF) measurements of liquid film thickness in annular flow, Part II: Analysis and comparison to models, Internation Journal of Multiphase Flow. 36:10 (2010) 825-835.
[8] D. Schubring, T. Shedd, E. Hurlburt, Studying disturbance waves in vertical annular flow with high-speed video, Internations Journal of Multiphase Flow, 36:5 (2010) 385-396.
[9] D. Steen, G. Wallis, AEC report, No. NYO-31142-2, 1964.
[9] X. Bai, T. Newell, Investgation of Two-Phase Viscous Liquid Flow, International Refrigeration and Air Conditioning Conference, Lafayette, Indiana, 2002.
[10] M. Alamu, B. Azzopardi, Simultaneous investigation of entrained liquid fraction, liquid film thickness and pressure drop in vertical annular flow, Journal of Energy Resources Technology. 133:2 (2011) 023103-1-10.
[11] R. Paz, O. Shoham, Film-Thickness Distribution for Annular Flow in Directional Wells: Horizontal to Vertical, Society of Petroleum Engineers, (1994) SPE-28541-MS.
[12] D. Butterworth, Air-water annular flow in a horizontal tube, Progress in Heat and Mass Transfer. 6 (1971) 235-251.
[13] A. Ansari, N. Sylvester, O. Sarica, O. Shoham, J.A. Brill, Comprehensive mechanistic model for upward two-phase flow in wellbores, SPE Production & Facilities. 9:2 (1994) SPE-20630-PA.

Ultra Compact Heat Exchanger With Geometry Induced Wall Jet

A K M M. Morshed Morshed (Bangladesh), Fazlul Bari (Bangladesh), Aashique Alam Rezwan Rezwan (Bangladesh)

Abstract:

Heat Exchanger (HX) is common but crucial equipment found in almost every engineering application which comes in different types, sizes and shapes. Performance of the HX is directly related with the overall system performance. Compactness of the HX is a good indication of its performance, usually the higher the compactness the higher the effectiveness. Increasing compactness of the HX by reducing the channel dimension is fairly a simple but highly effective technique. Although heat exchanger comprising of very small channel can achieve very high heat flux, its pumping requirement for circulating liquid increases very sharply. The pumping requirement can be reduced by increasing the number of channels either by vertical or horizontal stacking; the flow velocity through each channel is reduced for the same total mass flow rate of the liquid. In this study a novel technique called geometry induced wall jet is proposed to further enhance the performance of this heat exchanger comprising of small channels. The cross-flow from the wall jet disrupts the boundary layer of the channel flow enhancing the heat removal capacity of the heat exchanger. A CFD model has been developed using commercially available software package FLUENT to evaluate the overall thermal performance of this new design heat exchanger. A parametric study of the flow rates and the effect of the jet locations have been performed. Significant reduction in thermal resistance has been observed for proposed design.

Keywords: Heat Exchanger, Wall Jet, Heat Transfer Enhancemen

6th BSME International Conference on Thermal Engineering (ICTE 2014)

A study on multistage centrifugal pump performance characteristics for variable speed drive system

Rakibuzzaman[a], Sang-Ho Suh[a]*, Kim Kyung-Wuk[a], Hyung-Ho Kim[a], Min Tae Cho[b], In Sik Yoon[b]

[a]Dept.of mechanical Engineering, Soongsil University, Seoul, 156-743, South Korea
[b]Dooch Co., 295 Sagok-ri, Jangan-Myeon, Hwaseong-si, Gyeonggi-do, 445-942, South Korea

Abstract

Nowadays centrifugal pumps are being widely used in the commercial, industrial and power plant applications and most of pumps operated by constant speed drive system. Therefore, pump consumes a huge energy of each nation's total energy. But it could be operated in variable speed drive system which would be provided energy saving. The purpose of this study is to investigate the pump performance characteristics of the multistage centrifugal pump with the variable drive system. For this study an experimental set up of the system was constructed to achieve the centrifugal pump performances such as H-Q, η-Q, P-Q curves and operating points which interact between performance and system curves. In the variable speed drive system, a vector controlled inverter driving (variable voltage variable frequency) was installed in the experimental system. A numerical investigation also applied for getting the pump performances for the validation and reliability of the pump design development and also the pressure and velocity effects in internal flows of the pump are analyzed. For the numerical analysis, the Navier-Stokes equations were discretized by the finite volume method and two equations transport turbulence (SST) model accounts for three dimensional steady flows. In the experiment system, we also carried out system head performance of the three pumps in parallel to compare with one pump system head for its validation. In order to get the energy saving rate using the inverter control variable speed drive system instead of the constant speed drive system, it is necessary to identify the specific duty cycle of the pump operation cycle and operating system curve of the pump. Hopefully, this paper will be useful as a guide for identifying a method of implementing a variable speed drive system with inverter control in the variable flow and pressure system.

Keywords: Multistage centrifugal pump; Variable speed drive system; Inverter; Performance analysis; System curve; SST turbulence model;

* Corresponding author. Sang-Ho, Suh, Tel.: +82-2-820-0658; fax: +82-2-821-6758.
  E-mail address: suhsh@ssu.ac.kr

1. Introduction

A centrifugal pump is a type of fluid machine which is driven by a prime mover (e.g., an electric motor) used to impart energy to fluids, and continuously feed the required amount of such fluid to an intended height or distance [1]. The combination of rotating impeller and diffuser is called the stage. A multistage centrifugal pump might consist of several stages within a single housing, depending on the amount of pressure rise required of the pump [2].

According to statistics, pumps consume around 20% of the world total energy [3]. The energy efficiency of a system depends not only on the design of the pump but also, and more so, on its working conditions and system design [4,5]. The point of interaction is the only condition where the pump and system flow rates are equal and the pump and system heads are equal simultaneously. For the same type of pump operation, for one pump when the valve is fully open and flow rate compared with two or three pumps in parallel operation resulting to obtain the system curve. There are two driving systems. One is constant speed drive system which is installed with the pump and motor for transferring fluid. The other is variable speed drive system which is installed with pump, motor and inverter for changing speed. Inverter is a revolution control device which is used in the variable speed drive system [6, 7] and this control method is effectively used for pumps where operation time is long and output is high. Also energy savings are likely due to surface elevation and usually lower pumping rates and lower pipe friction losses can be obtained using variable speed drive system [5]. Assessment of the technical and economic advantages gained by using VSDs on centrifugal pumps have been a limited publicized in recent years. But with the performance and system curve we can't estimate satisfactory efficiency improvement using activated pump system. So, we have to find alternative method to evaluate the performance characteristics driving system.

Computational fluid dynamics (CFD) is being applied in the design of multistage centrifugal pump which can be used for numerical simulation to get the performance of the flow field inside the pump. CFD has proven to be a very useful tool in the analysis of the flow inside pumps, both in design and performance prediction. Much research has been carried out in the last years. Croba et al. [8] give an updated list of general selected papers while Denuset al. [9] give a more extended and specific bibliography. However, due to the difficulties of the task, most of these studies have been carried out with strong simplifications of the problem either in the geometry or in the flow characteristics. Research is slowly tending toward more complete simulations and approach developed follows the trend [10]. Numerical simulation makes it possible to visualize the flow condition inside a centrifugal pump, and provides the valuable hydraulic design information of the centrifugal pumps. For the numerical simulation in the pump, the main difficulty is to better reproduce the complex geometry configuration of the flow domain [11]. For these difficulties many of geometry are often considered for simplifications. In the literature, many hydrodynamics models are reported in 2D and 3D by using the CFD code and studied impeller diffuser interaction on the pump performance showed that a strong pressure fluctuation is due to the unsteadiness of the flow shedding from impeller [12, 13]. Both experimental and numerical approaches have been reported and have contributed to the understanding of the highly complex flow interactions that occur in a centrifugal pump [14].

In this paper, the study is focused on the pump performance characteristics of the multistage centrifugal pump with variable speed drive system. Therefore an experimental set up is constructed for both the one pump and three pumps in parallel. The pump performances were calculated by the electronic flow meter for the variable speed condition controlled by inverter. The system head curve calculated from both of one pump and three pumps in parallel. Also, we investigated the numerical simulation which predicts to get the pump performances and effect on pressure and velocity inside the pump. Thus these results compare with the experimental data for its effectiveness and reliability of the pump model DR 20-60.

2. Experimental Method

Fig. 1 shows the experiment layout of model pump and Fig. 2 represents the experiment layout of three pumps. The test layout is of the variable flow and pressure system. A fully computerized pump test facility is designed and built to obtain more accurate pump performance test data. Two electronic flow meters are used in the experiment system for better accuracy.

The working temperature and humidity were 28.5^0C and 81%. For each test, the rotational speed was set by the frequency inverter and the speed was measured by a torque meter showing in the pump operation panel. Pump head

was measured by algebraic difference height of liquid between the discharge and inlet sections. Pump shaft torque measured by torque meter which is connected to the signal amplifier. The mechanical power was measured as the product of shaft torque and angular velocity. Hydraulic power is given by the rate of mechanical energy input to the fluid. Efficiency was calculated as the ratio of hydraulic power to mechanical power.

In order to calculate the system head of one pump, the pump operated at constant speed with different flow rates and head data are taken. Then flow rate was fixed with the design flow rate and operated at full rotational speed that was 3600 rpm. Then gradually decreased the speed and flow rates and head were taken with the reduced speed. For the three pumps in parallel at first the one pump was operated with the design flow rate at constant speed and head data was taken. With the changing speed, flow rates and system head data were taken. Accordingly two pumps and three pumps were operated at the design flow rates and measured the system head. Pump head were measured with constant speed at different flow rates.
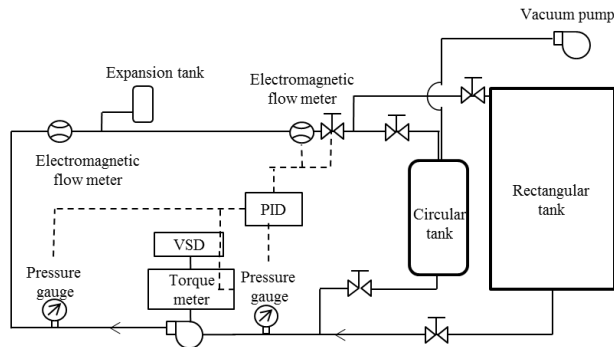

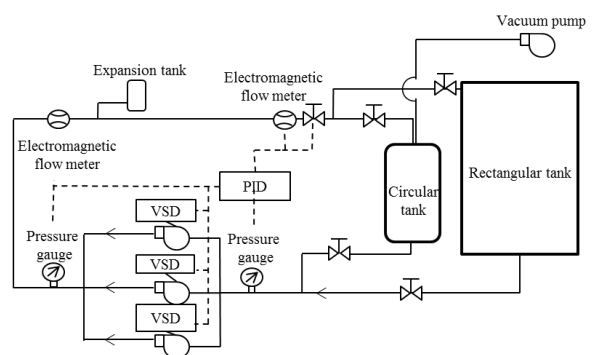Fig. 1 Experimental layout of the model pump

Fig. 2 Experimental layout of the three pumps in parallel

2.1. Pump performance evaluation

In order to evaluate the pump performance for both experiment and numerical simulation we need to calculate pump head, hydraulic power, mechanical power and hydraulic efficiency. In actual practice, hydraulic method and thermodynamic methods are applied to calculate the pump performances [15]. Hydraulic method was used in our performance investigation.

3. Numerical Method

To validate the experiment, computer simulation is conducted. The geometry of a six stage centrifugal pump impeller and diffuser were used for meshing by ANSYS ICEM-CFX-14.5 (Ansys Inc., 2012, USA). Each of impeller, diffuser, inlet casing, and outlet casing meshed with unconstructed tetrahedral cells which are shown in Fig. 3(a). The impeller had six blades and diffuser had ten blades. With the ANSYS ICEM-CFX surface mesh setup made, applied tetrahedral method, and computed mesh volume, and checked mesh quality. The total meshing grids were 5,265,401 nodes and 27,529,524 elements. Multistage centrifugal impeller domain was set up as rotating part and diffuser was considered as stationary domain. The model of a six stages multistage centrifugal pump considered in this study is shown in Fig. 3(b). To run the numerical simulation; we accounted the governing equations for centrifugal pump, the following assumptions were made: a three dimensional incompressible, steady-state flow, and the turbulence flow using the SST (shear stress transport turbulence) model was assumed as Newtonian fluid and the thermo-physical properties were constant with the temperature. To account for these assumptions, the theoretical analysis of the fluid flow was based on the continuity and momentum equations [16, 17]. The continuity and momentum equations are expressed as Eq. (1) and Eq. (2)

$$\frac{\partial u_i}{\partial x_i} = 0 \tag{1}$$

$$\rho(\frac{\partial u_i}{\partial t} + u_j \frac{\partial u_i}{\partial x_j}) = -\frac{\partial p}{\partial x_j} + \frac{\partial}{\partial x_j}(\mu \frac{\partial u_i}{\partial x_j} - \rho \overline{u_i' u_j'}) \qquad (2)$$

Where u_i is the velocity vector, p is the pressure scalar, ρ is the density, i and j is the tensor notations, $-\rho \overline{u_i' u_j'}$ is the apparent turbulent stress tensor, μ is the dynamic viscosity.

The k-ω based SST model accounts for the transport of the turbulent shear stress and highly accurate predictions of the onset and the amount of flow separation under adverse pressure gradients. The unknown turbulent viscosity μ_t is determined by solving two additional transport equations for the turbulent energy k, and for the turbulence frequency ω. These two equations can be written as Eq. (3) and Eq. (4)

$$\frac{\partial(\rho \kappa)}{\partial t} + \frac{\partial}{\partial x_j}(\rho \kappa u_j) = \frac{\partial}{\partial x_j}[(\mu + \frac{\mu_t}{\sigma_\kappa})]\frac{\partial \kappa}{\partial x_j} + P_k - \beta' \rho \kappa \omega + P_{kb}) \qquad (3)$$

$$\frac{\partial(\rho \omega)}{\partial t} + \frac{\partial}{\partial x_j}(\rho \omega.u_j) = \frac{\partial}{\partial x_j}[(\mu + \frac{\mu_t}{\sigma_\omega})]\frac{\partial \omega}{\partial x_j} + \alpha \frac{\omega}{\kappa}P_k - \beta \rho \omega^2 + P_{\omega b}) \qquad (4)$$

Where, P_k is the production rate of turbulence, μ_t is the turbulent viscosity, α, β, β', σ_k and σ_ω are constants.
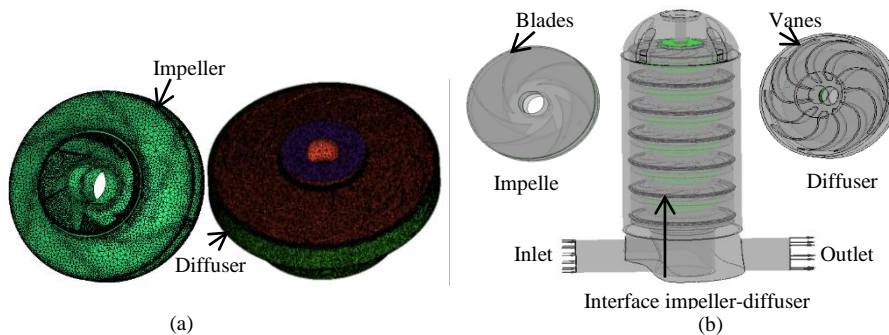

Fig. 3 (a) Meshing of impeller and diffuser; (b) impeller-diffuser domain interface

4. Results and discussion

4.1. Model validation of the experimental study

In order to validate the numerical approach, a comparison of the experimental and the computed data were carried out. Fig. 4 shows the pump head, efficiency and power of the system used of different flow rates with different rotational speed. From this graph its being shown a good agreement between the experiment and numerical data so that the average deviation of the head values was only 5.4%. The highest deviation found of 11.06% for the highest flow rate at 3050 rpm and the differences for only three conditions are larger than 8.5%. Along with the decreases of the rotational speed the head is being continuously decreased. The numerical methods predict the pressure rise more accurately compared with the experimental data. After that, the pump efficiency shows an average deviation in only 8.22%, and the highest deviation is 13.12% for the highest flow rate of 3600 rpm. Also, the pump shaft power average deviation was only 6.35%. The Fig. 4 shows a small deviation of the numerical data and follows the trend of the experimental results**.**

4.2. Pump operating characteristics

Basically, a pump system would be required to run at the operating point, the head is rise with the flow rate and
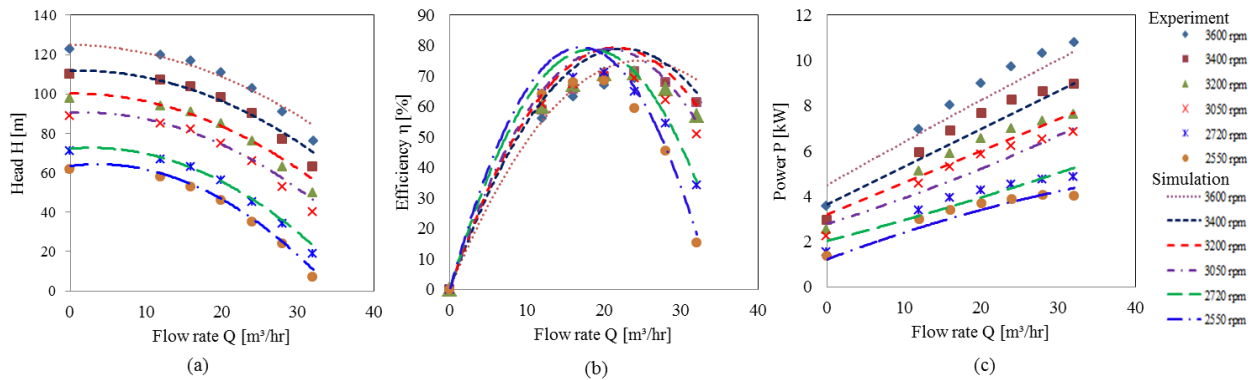
Fig. 4 Comparisons of experiment versus numerical performance curve of the multistage centrifugal pump (a) head (H) vs flow rate (Q); (b) efficiency (η) vs flow rate (Q); and (c) power (P) vs flow rate (Q)

required system head match. A single pump performance system curve is shown in Fig. 5(a). This system shows the system curve at the rated flow rate. For the rated flow rate pump curve determine the maximum operating point of the pump rate at 36.8 m^3/hr. With the full open controlled valve the system head loss is small and H-Q curve not intersect the system curve. The operating point would be determined by the intersection of the pump curve and the system curve. With the controlled valve the pump curve is reduced by reducing the pump speed and the reduced pump speed can be obtained by the centrifugal pump laws. At that operating point the designed flow rate was 24 m^3/hr at 103.31m head. The operating point moves down the system curve with the result that flow and head are reduced accordingly controlled speed.

With the variable rotational speed the system curve would be cut the different pump head and the operation point of the pump can be operated below the constant drive pump. The difference in pressure between operating along the rated flow pump curve and the system curve represents the potential energy saving because of the valve losses Fig. 5(b) represents the operating characteristics of pump head curve and system curve of three pumps in parallel. In this figure, with the one pump the operating point is at the best efficiency point at the design flow rate at maximum
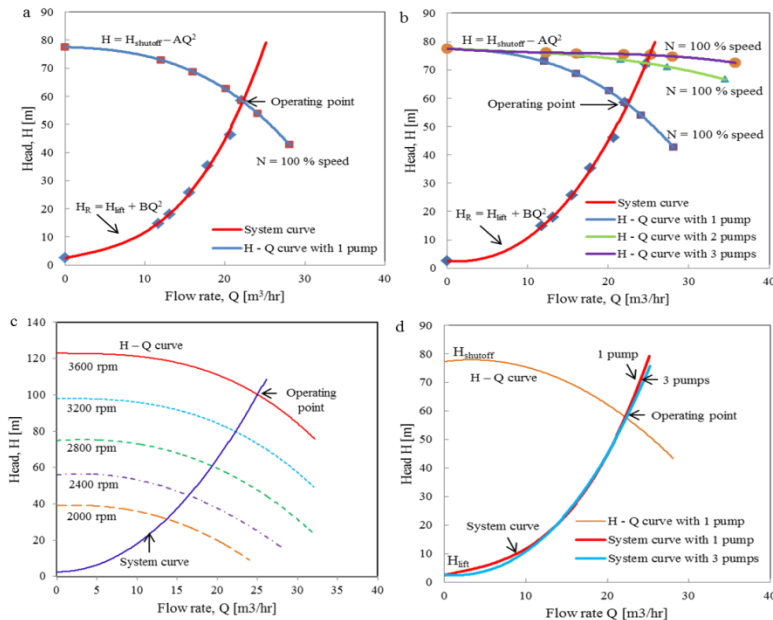

Fig. 5 (a) inverter controlled variable flow and pressure system characteristics; (b) operating characteristics of three pumps; (c) System head for model pump (d) system head for one pump and three pumps.

rotational speed (3600 rpm). The system head is done by varying the different speeds. With the two pumps in operation at full speed the system head is increases as well as the pump head and flow rate increased. The pump head and the system head matched at the 2Q flow rates. For three pumps, the operating point matched at 3Q flow rates and head is slightly increases. The system curve is intersecting at just above the second pumps head. Fig. 5(c) shows the inverter drive control system curve of model pump. Fig. 5(d) represents the comparison of one pump and three pumps in parallel for the model pump system curve for validation. The system head for model pump is almost same of the three pumps system head in parallel.

5. Conclusion

The study is based on the inverter controlled variable speed drive multistage centrifugal pump in a closed loop variable flow and pressure system. A model pump was installed in designed layout to achieve the performance for the constant and variable speed drive conditions. The result of this system indicates that the energy saving could be obtained when the similar type of pumps would be running at same speed ratio. For variable speed drive pump indicates, the operating point moves down the system curve with the result that flow and head are reduced accordingly controlled speed. But in case of constant drive pump, the operating point moves forward to the head curve as a result that flow is reduced and head is increased. The point of interaction of operating point is the only condition where the pump and system flow rates are equal and the pump and system head are equal simultaneously. This intersection would generally be chosen to ensure that the pump is operated at or near its best efficiency point. Three pumps system curve are considered for model pump system curve validation.

The potential applications for variable speed drive with inverter control system represents a potential energy saving and it can be used a numerous in the domestic and industrial sectors. The system would be improved performance and life cycle of the pump because of low pressure.

Acknowledgements

References

[1] Pumping station engineering hand book, Japan association of agriculture engineering enterprises, Tokyo, (1991) 21.
[2] Fox, R., et al., Fluid Mechanics, John Wiley and Sons Inc., Asia, (2012), 494-541.
[3] D. kaya et al., Energy efficiency in pumps, Energy Conversation and Management, 49 (2008), 1662-1673.
[4] Metehan K., Murat A., Efficient driving at variable speeds, World Pumps April 2013.
[5] Armintor, J. K., and D. P Conners, Pumping Applications in the Petrolium and Chemical Industrys, IEEE Transac-tions on Industry Application, 23 (1) (1987) 43-48.
[6] Bimal, K. B., Modern Power Electronics and AC Drives, Prentice Hall Inc., (2002) 29-97.
[7] Pumping station engineering hand book, Japan Association of Agriculture Engineering Enterprises, Tokyo, (1991) 297-321.
[8] Croba, D. et al., Numerical Calculation of 2D, Unsteady Flow in Centrifugal Pumps: Impeller and Volute Interaction, International Journal for Numerical Methods in fluids, 22 (1996) 467- 481.
[9] Denus, C. K. and Go de, E., A Study in Design and CFD Analysis of a Mixed-Flow Pump Impeller, ASME-FEDSM (1999), 99-6858.
[10] Miner, S. M., Evaluation of Blade Passage Analysis Using Coarse Grids, ASME J. Fluids Eng., 122 (2000) 345–348.
[11] Hedi, M.L., Hatem, K. et al., Numerical analysis of the flow through in centrifugal pumps, International Journal of thermal Technologies, 2 (4) (2012) 216-221.
[12] Shum, Y. K. P. et al., Impeller-diffuser interaction is a centrifugal compressor, Journal of Turbomachinery , 122 (4) (2000) 777-786.
[13] Akhras, A. et al., The flow rate influence on the interaction of a radial pump impeller and the diffuser, International Journal of Rotating Machinery, 10 (4) (2004) 309-317.
[14] Gonzalez, J., Fernandez, J. et al., Numerical simulation of the dynamics effects due to impeller-volute interaction in a centrifugal pump, ASME J. Fluids Eng., 124 (2002) 348–355.
[15] ISO 5198: 1987 (E), Centrifugal, mixed flow and axial pumps-code for hydraulic performance tests-precision class, International Standard.
[16] F. M. White, Viscous Fluid Flow, McGraw Hill, second ed., New York, 1991.
[17] Ansys Inc. 2012. ANSYS-CFX (CFX Introduction, CFX Reference guide, CFX Tutorials, CFX-Pre User's Guide, CFX-Solver Manager User's Guide, Theory Guide), re-lease 14. 5, USA.